

# Dynamical phase transitions in the fully connected quantum Ising model: Time period and critical time

Arun Sehrawat<sup>1,2,\*</sup>, Chirag Srivastava<sup>1,†</sup> and Ujjwal Sen<sup>1,2,‡</sup>

<sup>1</sup>Harish-Chandra Research Institute, HBNI, Chhatnag Road, Jhunsi, Allahabad 211019, India

<sup>2</sup>QpiAI India Pvt Ltd, WeWork, Manyata NXT Tower 1, Embassy Manyata Business Park, Nagavara, Bengaluru 560045, India



(Received 31 December 2020; revised 11 July 2021; accepted 13 July 2021; published 4 August 2021)

We study dynamical properties of the finite-size fully connected Ising model with a transverse field at zero temperature. In a quench dynamics, we study the time period and the first critical time, which play important roles in the dynamical phase transitions, based on a dynamical order parameter and the Loschmidt rate, respectively. When all the spins are initially polarized in the direction of their mutual interaction, we show that both the time period and critical time diverge logarithmically with the system size at the dynamical critical point. When all the spins are initially in the direction of transverse field, both the time period and critical time exhibit logarithmic or power-law divergences depending on the final field strength. In the case of convergence, we provide estimates for the finite-size scaling and converged value. We also investigate the equilibrium phase transition, presenting approximate ground and first excited states away from the criticality, and compare their energy gap and bipartite and multipartite entanglements with the exact eigenstates.

DOI: [10.1103/PhysRevB.104.085105](https://doi.org/10.1103/PhysRevB.104.085105)

## I. INTRODUCTION

Quantum phase transitions are one of the most fascinating phenomena that emerge in many-body systems at zero temperature in the thermodynamic limit [1]. In this paper, we study phase transitions for the fully connected Ising model (FCIM) with a transverse magnetic field, where “fully connected” means every spin interacts with every other spin. The FCIM is a special case of the Lipkin-Meshkov-Glick (LMG) model [2–4] and is related to the two-component Bose-Einstein condensates [5,6]. Ferromagnetic to paramagnetic equilibrium phase transition occurs in the FCIM as we increase the field strength from zero to infinity. The transition can be described by adopting a mean-field approach [7–9] (see also [5]).

The finite-size scaling analysis of [10] is extended in [7,8] for the LMG model, and it is shown how the magnetization and energy gap approach their mean-field values as the system size grows. At the critical point, they go to zero with a *power law*. One needs to go beyond mean-field theory to capture entanglement properties such as concurrence [11,12] and geometric entanglement [13–27] of the ground state. The rescaled concurrence develops a cusplike singularity at the critical point with a power law [28–31]. Whereas, the geometric entanglement [21], entanglement entropy [32–34], and mutual information [35] of the ground state diverge *logarithmically* with system size at the phase transition point. The finite-size scaling exponents for two-body correlations are obtained in [30,36] for the LMG model.

In Sec. II, we briefly consider certain aspects of the equilibrium phase transition of the FCIM, which among other things provide easy reference for the later parts of the paper on dynamical phase transitions.

In Sec. III, we investigate dynamical phase transitions (DPTs) in the FCIM through a quantum quench, where a value of a Hamiltonian parameter (the transverse field strength in our case) is abruptly changed, and thus the system goes out of equilibrium and the dynamics begin. Broadly, the DPTs are of two kinds, viz., the first and second kinds (DPT-I [9,37–61] and DPT-II [51,57,59–79]) and are based on a certain dynamical order parameter and the Loschmidt rate function, respectively. In the case of FCIM, the equilibrium phase transition and DPTs are distinct phenomena and their critical points are different [52,60,75,77]. Recently, DPTs have been experimentally realized in [55–57,62] for the FCIM and LMG model, and in [58] for the collective Heisenberg model. It should be noted that the name “dynamical phase transition” has been used also for phenomena somewhat independent of the one considered in this paper [80–84].

Like an equilibrium phase transition, two phases in a DPT-I are associated with nonzero and zero values of a dynamical order parameter, and how it goes to zero at the critical point determines the nature of the transition. The DPT-I in the Fermi-Hubbard model [42–44], Bose-Hubbard model [45–47], Jaynes-Cummings model [47], quantum  $\phi^4$   $N$ -component field theory [48], films [49], and in the FCIM [9,47,50–54] are described through classical (mean-field) equations of motion in the thermodynamic limit, where an order parameter oscillates around its time-averaged value with a time period. The averaged value is called the *dynamical* order parameter. Furthermore, it is known that the time period and dynamical order parameter, respectively, go to infinity and zero *logarithmically*, in contrast to the equilibrium phase

\* arunsehrawat2@gmail.com

† chiragsrivastava@hri.res.in

‡ ujjwal@hri.res.in

transitions, as functions of the Hamiltonian parameter at the dynamical critical point. We shall see in Sec. III A 1 that these two physical quantities are inversely proportional to each other in the FCIM [53], and the time period diverges logarithmically with the system size at the critical point, which is one of our contributions.

In the case of DPT-II, the Loschmidt rate, as a function of time and the Hamiltonian parameter, is a dynamical counterpart of the free-energy density, and a sharp change in its behavior indicates a phase transition [63,79]. The change can be observed with respect to the Hamiltonian parameter (for example, see [60,75]) or related to time [59,62].

If one examines the behavior of Loschmidt rate (considering all the times) with respect to the Hamiltonian parameter, then she will observe the regular and anomalous phases when the quenching is from the ferromagnetic phase and will observe the regular and trivial phases when it is from the paramagnetic phase in the FCIM [60,75,76] (for further analyses, see [51,61,77,78]). Sections III A and III B separately deal with the quantum quenching from the ferromagnetic and paramagnetic phases, respectively. In each of these sections, we study the DPT-I and DPT-II sequentially.

For a fixed Hamiltonian-parameter value, the rate can show a series of kinks or cusps (nonanalyticities) at the so-called critical times. There is no cusp in the trivial phase. The regular and anomalous phases have the first cusp before and after the first minimum of the rate function, respectively. In this paper, we study the *first* critical time (when the first kink occurs). The time period and the critical time share a close relationship [51,59,60,62,63,77]. In Sec. III, as a set of results, we essentially show that both the time period and the first critical time have the same diverging behavior (logarithmic or power law) with respect to system size at the critical points. In a convergent case, we provide estimates for the finite-size scaling and converged value for both the time period and critical time. Our main results are highlighted at the beginning of each section, and a summary is presented in Sec. IV. Appendices carry supplementary material.

## II. APPROXIMATE GROUND AND EXCITED STATES AND THEIR ENTANGLEMENTS

In this section, as our first result, we provide justifications for (5), which basically says that for a finite system, the approximate energy eigenkets  $|\chi\rangle$  of (4) are better than the mean-field approximations of the exact energy eigenkets  $|e\rangle$  except near the phase transition point. Our justifications are based on the numerical data plotted in Figs. 13–16. As our second contribution, we capture the entanglement properties of  $|e\rangle$  through  $|\chi\rangle$ , which are presented in (6) and (7), and in Figs. 1 and 2. Moreover, the result in (8) and the figures about the entanglement of first excited state are also new. Now we begin our analysis.

For a system of  $N$  spin- $\frac{1}{2}$  particles,  $S_\eta := \frac{1}{2} \sum_{i=1}^N \sigma_i^\eta$  specifies the total angular momentum in the direction  $\eta = x, y, z$ , where the Pauli operator  $\sigma_i^\eta$  acts on the  $i$ th spin only. The Hamiltonian of the FCIM with a transverse field is given by

$$H = -\frac{\Gamma}{2N}(S_z)^2 - h S_x, \quad (1)$$

where  $\Gamma$  and  $h$  are the two-body interaction and transverse-field strengths, respectively. Throughout the paper, we fix the temperature to be zero and  $\Gamma = 1$ , and we work with  $h$  as the control parameter. Since  $N = 2j$ , the thermodynamic and classical limits are the same in the FCIM. In the limit, one can find the ground-state energy per particle by minimizing [5,7–9,30,85]

$$\begin{aligned} \mathcal{E}_h(\theta, \phi) &:= \lim_{j \rightarrow \infty} \frac{\langle \theta, \phi | H | \theta, \phi \rangle}{j} \\ &= -\frac{1}{4}(\cos \theta)^2 - h \sin \theta \cos \phi \end{aligned} \quad (2)$$

over  $\theta \in [0, \pi]$  and  $\phi \in [0, 2\pi]$ , where  $|\theta, \phi\rangle$  is the spin coherent ket [86] expressed in (A3).

The two coherent kets  $|\theta_0, \phi_0\rangle$  and  $|\pi - \theta_0, \phi_0\rangle$  provide the minimum energy  $\mathcal{E}_h(\theta_0, \phi_0)$ , where

$$(\theta_0, \phi_0) = \begin{cases} (0, \phi_0) & \text{for } h = 0, \\ (\arcsin(2h), 0) & \text{for } 0 < 2h \leq 1, \\ \left(\frac{\pi}{2}, 0\right) & \text{for } 1 \leq 2h < \infty. \end{cases} \quad (3)$$

Since  $\phi_0$  does not depend on the parameter  $h$ , we omit it from the kets in the following. One can observe that the kets are distinct (double-degenerate ground state) in the ferromagnetic phase characterized by  $0 \leq 2h < 1$ . While, they become the same at the equilibrium phase transition point  $h^{\text{eq}} = \frac{1}{2}$  and remain so in the whole paramagnetic phase specified by  $1 < 2h$ . This reveals that the ground state is nondegenerate in the paramagnetic phase.

One can easily describe the phase transition in FCIM through the above mean-field analysis [5,7–9,30,85], but one can not capture the entanglement properties of ground state through  $|\theta_0\rangle$  and  $|\pi - \theta_0\rangle$  as they are product kets [30]. Moreover, they are not good approximations of the ground state when  $j$  is finite as shown below. Although, the exact energy eigenstates, based on the Bethe ansatz, are known [87], but they are rather complicated. So all these things motivate us to find the approximate energy eigenstates that are simple to express, better than the two coherent states, and captures the entanglement properties. Once we have such states then it is straightforward to compute the expectation value of any physical quantity that we desire.

In Appendix A, we provide justifications for choosing

$$\begin{aligned} |\chi_{\pm}\rangle &:= \frac{|\theta_0\rangle \pm |\pi - \theta_0\rangle}{\sqrt{2[1 \pm (\sin \theta_0)^N]}} \quad \text{for } 0 \leq 2h < 1 \quad \text{and} \\ |\chi_0\rangle &:= \cos \frac{\mu_0}{2} |j\rangle_x + \sin \frac{\mu_0}{2} |j-2\rangle_x, \\ |\chi_1\rangle &:= \cos \frac{\mu_1}{2} |j-1\rangle_x + \sin \frac{\mu_1}{2} |j-3\rangle_x \quad \text{for } 1 \leq 2h \end{aligned} \quad (4)$$

as approximate energy eigenstates that met the above requirements. The subscripts 0 or + and 1 or – are associated with the ground and first excited states, and the exact eigenkets of  $H|e_{0,1}\rangle = e_{0,1}|e_{0,1}\rangle$  are obtained numerically. The parameters  $\mu_{0,1}$  are derived in Appendix B. One can intuitively understand properties of the above kets:  $|\chi_{\pm}\rangle$  are like the GHZ (or Schrödinger-cat) kets [5,88], whereas  $|\chi_{0\text{ or }1}\rangle$  is a superposition of two Dicke kets.

In Figs. 13 and 14, we plot the overlaps between  $|\chi\rangle$  and  $|e\rangle$  that show the following: first, for a finite system,  $|\chi_{+,0}\rangle$  are

better than the mean-field approximations  $|\theta_0\rangle$  and  $|\pi - \theta_0\rangle$  of the ground-state vector  $|e_0\rangle$ . Second, overall  $|\chi\rangle$  are good approximations of  $|e\rangle$  except near the phase transition point, hence, we can assert that

$$|e_0\rangle \approx \begin{cases} |\chi_+\rangle & \text{for } 0 < h < \frac{1}{2} - \delta \\ |\chi_0\rangle & \text{for } \frac{1}{2} + \delta < h \\ & \text{while } |\chi_-\rangle \end{cases} \approx |e_1\rangle, \quad (5)$$

where we put a small number  $\delta > 0$  to exclude  $h$  values near the critical point. This is our first result of the section. Furthermore, the approximate energy gap based on  $|\chi\rangle$  of (4) also matches well with the actual gap  $e_1 - e_0$  for all  $h$  except in a small interval around the transition point (see Fig. 16).

Now, we compare the entanglement properties of  $|e\rangle$  and its approximation  $|\chi\rangle$ . The concurrence  $C := \max\{0, \sqrt{\lambda_m} - \sum_{\lambda \neq \lambda_m} \sqrt{\lambda}\}$  measures two-body entanglement [11,12], where  $\lambda \geq 0$  are the eigenvalues of  $\rho \tilde{\rho}$ , and  $\lambda_m = \max\{\lambda\}$ . The two-body density matrix  $\rho$  is obtained here from a  $N$ -body quantum state by taking trace over all spins except the two between which we are measuring the entanglement, and  $\tilde{\rho} = (\sigma^y \otimes \sigma^y)\rho^*(\sigma^y \otimes \sigma^y)$ , where  $\rho^*$  is the complex conjugate of  $\rho$ .

We have numerically computed the concurrence of  $|e_{0,1}\rangle$  by exploiting a result (C1) from [89] and presented it in Fig. 1. In Appendix C, we work out analytical formulas of the concurrence for  $|\chi_{\pm}\rangle$  as well as  $|\chi_{0,1}\rangle$ , and they are

$$\begin{aligned} C_{\chi_{\pm}} &= \frac{(\cos \theta_0)^2 (\sin \theta_0)^{N-2}}{1 \pm (\sin \theta_0)^N}, \\ NC_{\chi_0} &= \sqrt{2} \sin \mu_0 + 2 \cos \mu_0 - 2 \quad \text{for } N \gg 1, \\ \lim_{N \rightarrow \infty} (NC_{\chi_0}) &= \frac{(8h-1)}{\sqrt{(4h-1)^2 + \frac{1}{2}}} - 2, \\ NC_{\chi_1} &= 4 - 2 \left( \cos \mu_1 + \sqrt{6} \sin \frac{\mu_1}{2} \right) \quad \text{for } N \gg 1, \\ \lim_{N \rightarrow \infty} (NC_{\chi_1}) &= 4 - 2 \left( \frac{(4h-1)}{\sqrt{(4h-1)^2 + \frac{3}{2}}} \right. \\ &\quad \left. + \sqrt{3} \sqrt{1 - \frac{(4h-1)}{\sqrt{(4h-1)^2 + \frac{3}{2}}}} \right). \end{aligned} \quad (6)$$

Taking  $\theta_0$  from (3), we have  $C_{\chi_{\pm}}$  as functions of the system size  $N$  and the field strength  $h \in [0, \frac{1}{2}]$ .  $C_{\chi_{\pm}}$  decay exponentially with  $N$  due to the factor  $(\sin \theta_0)^{N-2}$ , however, both show sharp peaks near the phase transition point when  $N$  is large (see Fig. 1) and  $\lim_{h \rightarrow 1/2} (NC_{\chi_-}) = 2$ . Taking  $\mu_{0,1}$  from (B3)–(B5), we gain the concurrences  $C_{\chi_{0,1}}$  as the functions of  $N$  and  $h$  in (6).

Since every spin is interacting with all the others, the two-body entanglement gets diluted (due to the monogamy of entanglement [90,91]), hence the rescaled concurrence  $NC$  will provide the nontrivial information about the two-body entanglement [28]. So, in Fig. 1, all the plots display  $NC$ . There one can observe that the concurrences of  $|e\rangle$  and  $|\chi\rangle$  match well when either  $j$  is small or in the paramagnetic phase away from the transition point.

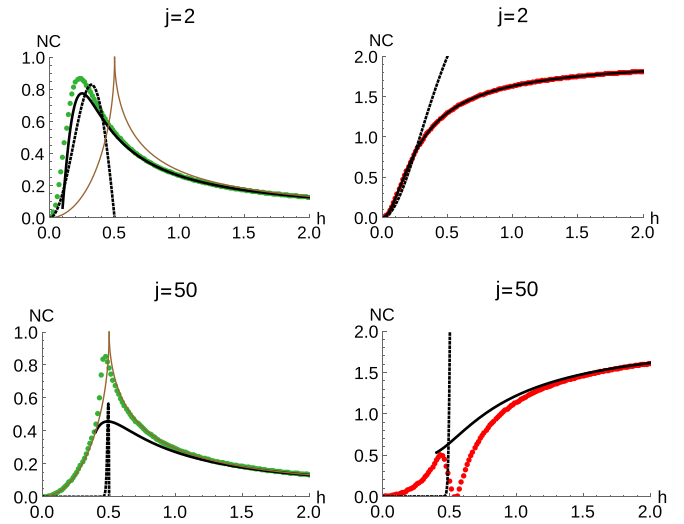


FIG. 1. Rescaled concurrence versus field strength. The green and red points on the left- and right-hand sides depict the rescaled concurrences  $NC$  for the exact ground-state  $|e_0\rangle$  and first-excited-state  $|e_1\rangle$  vectors, respectively. The black dotted and continuous curves represent  $NC$  [from (6), (C10), and (C12)] for  $|\chi_{+-}\rangle$  and  $|\chi_{0,1}\rangle$ , respectively. The brown curves illustrate the rescaled concurrence  $1 - \sqrt{1 - (2h)^2}$  for  $0 \leq 2h \leq 1$  and  $1 - \sqrt{1 - (2h)^{-1}}$  for  $1 \leq 2h$  given in [30] for  $|e_0\rangle$  in the thermodynamic limit.

Next, we consider the geometric measure of entanglement [13–27], which for a pure state  $|\chi\rangle\langle\chi|$  is defined by  $G_\chi := 1 - \max_{|\vartheta\rangle\langle\vartheta|} |\langle\vartheta|\chi\rangle|^2$ , where the maximum is taken over all the product states  $|\vartheta\rangle\langle\vartheta| := \otimes_{i=1}^N |\vartheta_i\rangle\langle\vartheta_i|$ . We numerically found the maxima of  $|\langle\vartheta|e\rangle|^2$  and  $|\langle\vartheta|\chi\rangle|^2$  and the values of  $\vartheta$  where they occur (for details, see Appendix D). Then,  $G_e$  and  $G_\chi$  with the  $\vartheta$  values are presented in Fig. 2. One can observe a good match between  $G_e$  and the corresponding  $G_\chi$  for all  $j \geq 10$  and  $h \geq 0$  except near the phase transition point.

In the ferromagnetic phase, both  $G_{e_{0,1}}$  stay close to  $\frac{1}{2}$ , which is the geometric entanglement of the GHZ states [17] that are similar to  $|\chi_{\pm}\rangle$ . In the paramagnetic phase,  $G_{e_0}$  drops to zero while  $G_{e_1}$  becomes slightly more than one half. When  $h \rightarrow \infty$ , both  $|e_1\rangle$  and  $|\chi_1\rangle$  turn into the w-ket  $|j-1\rangle_x$  [92], whose geometric entanglement  $G_{\chi_1} = 1 - (\frac{N-1}{N})^{N-1}$  [17] is indicated by the blue point at  $h = 1$  in Fig. 2. In Appendix D, we also obtain

$$\begin{aligned} G_{\chi_{\pm}} &= \frac{1}{2}(1 \mp (2h)^N) \quad \text{for } N \gg 1, \\ G_{\chi_0} &= 1 - \left( \cos \frac{\mu_0}{2} \right)^2. \end{aligned} \quad (7)$$

In Fig. 18 placed in Appendix D, we present the rescaled concurrence  $NC_{e_{0,1}}$  and geometric entanglement  $G_{e_{0,1}}$  for both  $|e_{0,1}\rangle$  at the critical point. The best-fitted functions in the figure suggest the large- $j$  scalings

$$\begin{aligned} 1 - NC_{e_{0,1}} &\sim j^{-\frac{1}{3}}, & 1 - G_{e_0} &\sim j^{-\frac{1}{6}}, \\ 1 - G_{e_1} &\sim j^{-0.12}, & \text{and } \frac{\pi}{2} - \vartheta &\sim j^{-0.35} \end{aligned} \quad (8)$$

in the case of  $|e_1\rangle$ . The numbers 0.12 and 0.35 are the estimated scalings based only on the numerical data in the figure.

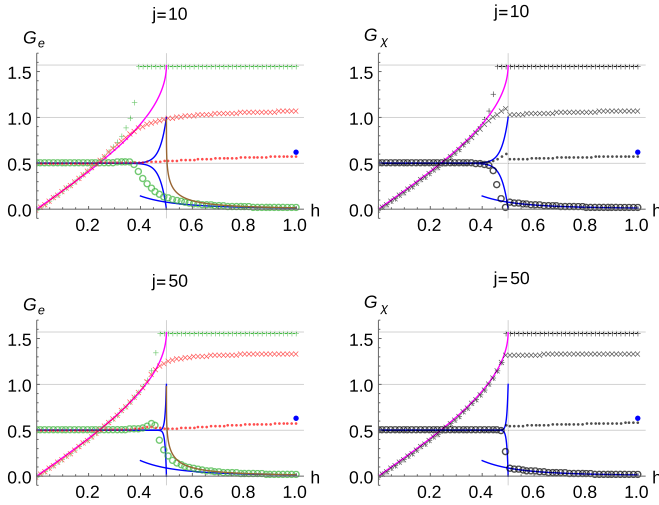


FIG. 2. Geometric entanglement versus field strength. In the left and right columns, we display the geometric entanglement for the exact and approximate eigenstates, respectively. The green (black) circles and red (black) dots depict  $G_e$  ( $G_x$ ) of  $|e_0\rangle$  ( $|\chi_{+or0}\rangle$ ) and  $|e_1\rangle$  ( $|\chi_{-or1}\rangle$ ), respectively. The three blue curves illustrate  $G$  of (7). A green (black) “+” mark shows the value of  $\vartheta$  where  $|\langle\vartheta|e_0\rangle|^2$  ( $|\langle\vartheta|\chi_{+or0}\rangle|^2$ ) reaches its maximum value. The plus marks closely follow the magenta curve, that highlights  $\theta_0 = \arcsin(2h)$ , in the range  $h \in [0, \frac{1}{2}]$  and follow  $\frac{\pi}{2}$  when  $1 \leq 2h$ . A green (black) “ $\times$ ” indicates  $\vartheta$  where  $|\langle\vartheta|e_1\rangle|^2$  ( $|\langle\vartheta|\chi_{-or1}\rangle|^2$ ) attains its highest value. The cross marks also follow the magenta curve near the phase transition point, and then they deviate and saturate to a value. The saturated value changes with  $j$ . In the left plots, the brown curve exhibits  $1 - \sqrt{1 - (\sqrt{2h} - \sqrt{2h-1})^4}$ , which is derived from Eqs. (4)–(6) in [21] for  $1 \leq 2h$  and  $j \gg 1$ .

It is interesting to see that  $G_{e_1} \rightarrow 1$  at the critical point is captured by  $\lim_{2h \rightarrow 1^-} G_{\chi_-} = 1$  in (7). The results in (8) for the ground-state vector  $|e_0\rangle$  are already known [21,28–30].

### III. DYNAMICAL PHASE TRANSITIONS: TIME PERIOD AND CRITICAL TIMES IN THE QUENCH DYNAMICS

The dynamical phase transitions (DPTs) [9,37–79], emerge in the evolution induced by a quantum quench, where the system is initially prepared in the ground state  $|\psi_{\text{in}}\rangle = |e_0\rangle$  of the Hamiltonian  $H(h_{\text{in}})$ . At the time  $t = 0$ , the field magnitude is suddenly changed from  $h_{\text{in}}$  to  $h_f \neq h_{\text{in}}$ , which begins the dynamics narrated by

$$|\psi(t)\rangle = e^{-iH_f t} |\psi_{\text{in}}\rangle, \quad (9)$$

where  $H_f := H(h_f)$ . Without loss of generality, we take both  $h_{\text{in}}, h_f \geq 0$ .

The DPT-I is based on a dynamical order parameter, which in our case (in the following sections) is related to the spin vector

$$\begin{aligned} \mathbf{s}(t) &:= \frac{1}{j} \langle \psi(t) | \mathbf{S} | \psi(t) \rangle = \mathbf{s}_{\text{cl}}(t) + O\left(\frac{1}{j}\right), \\ \mathbf{s}_{\text{cl}}(t) &:= (\sin \theta \cos \phi, \sin \theta \sin \phi, \cos \theta), \end{aligned} \quad (10)$$

where  $\mathbf{S} = (S_x, S_y, S_z)$ . In the classical limit, from the Heisenberg equation of motion for  $\mathbf{S}$ , one gets [9,47,61]

$$\begin{aligned} \frac{d\theta}{dt} &= h_f \sin \phi, \\ \frac{d\phi}{dt} &= -\frac{1}{2} \cos \theta + h_f \cot \theta \cos \phi \end{aligned} \quad (11)$$

for the unit vector  $\mathbf{s}_{\text{cl}}$ . After the quench, the energy remains conserved,

$$\mathcal{E}_{h_f}(\theta(t), \phi(t)) = \mathcal{E}_{h_f}(\theta_{\text{in}}, \phi_{\text{in}}), \quad (12)$$

for all  $t \geq 0$  [for  $\mathcal{E}$ , see (2)]. The initial values  $(\theta_{\text{in}}, \phi_{\text{in}})$  are fixed by  $h = h_{\text{in}}$  as per (3) and (12).

The so-called DPT-II is based on the Loschmidt rate function [63,79]

$$r_{\infty}(t) := \lim_{N \rightarrow \infty} r(t), \quad \text{where}$$

$$r(t) := \frac{1}{N} \ln \left( \frac{1}{p(t)} \right), \quad p(t) := |\langle \psi_{\text{in}} | \psi(t) \rangle|^2 \quad (13)$$

is the probability (known as the Loschmidt echo) of returning to the initial state. In the DPT-II, we study the so-called critical times when kinks, measured by discontinuities in the first derivative of  $r$  with respect to time, appear in  $r(t)$ . In Secs. III A and III B, we consider  $h_{\text{in}} = 0$  (quench from the ferromagnetic phase) and  $h_{\text{in}} \rightarrow \infty$  (quench from the paramagnetic phase) separately.

#### A. Initially all spins are up in the $z$ direction

Throughout this section, we fix  $h_{\text{in}} = 0$ . Hence, for every  $N$ , Hamiltonian (1) has two minimum energy eigenkets  $|\pm j\rangle_z$ , out of which we choose  $|\psi_{\text{in}}\rangle = |+j\rangle_z$ . It means, initially, all the spins are up in the  $z$  direction and  $\theta_{\text{in}} = 0$ .

#### I. DPT-I

Let us first consider the DPT-I. The results between (14) and (19) have been known through [9,47,50–53,60], and similar calculations are reported in [42–44,46,48,49] for other mean-field models. In this section, our main results are in Table I, the bottom-right plot in Fig. 4, (21), and (22). They basically show how the time period denoted by  $T$  varies with the system size for different  $h_f$ .

Here the energy conservation (12) becomes

$$\sin \theta = (4h_f) \cos \phi, \quad (14)$$

which determines  $\phi_{\text{in}} = \frac{\pi}{2}$  as per  $h_f > 0$ . By taking the top and bottom equations of (11) for  $1 < 4h_f$  and  $4h_f < 1$ , separately, one can reach their solutions

$$\begin{aligned} F(\theta | (4h_f)^{-2}) &= h_f t \quad \text{for } 1 < 4h_f, \\ F\left(\frac{\pi}{2} - \phi \middle| (4h_f)^2\right) &= \frac{1}{4} t \quad \text{for } 4h_f < 1 \end{aligned} \quad (15)$$

with the help of (14), where

$$\begin{aligned} F(\gamma | k^2) &:= \int_0^\gamma \frac{dw}{\sqrt{1 - (k \sin w)^2}}, \\ K(k^2) &:= F\left(\frac{\pi}{2} \middle| k^2\right) \end{aligned} \quad (16)$$

TABLE I. The best-fit functions for the half-time period. For  $h_{\text{in}} = 0$ , the best-fit functions  $g(j)$  for  $\{\frac{T_j}{2}\}$  are recorded here with the obtained minimum  $\chi^2$  “error” of (E2). The numbers such as  $18.23 \pm 1$  represent the 95% marginal confidence intervals as per (E5), where 18.23 and 1 denote the maximum likelihood estimator and the error bar, respectively, for the fitting parameter. In all other tables, the estimated parameters are also presented in this fashion, and they are obtained by following the least-squares method of Appendix E. Throughout the paper, to plot  $g$  as a function of  $j$ , we have taken it without the error bars. The time period  $T_{\text{cl}}$  comes from (19). Both the  $g$  functions for  $h_f = 0.3$  deliver almost the same plot in Fig. 4.

$h_f$	$\frac{T_{\text{cl}}}{2}$	$g(j)$	error
0.2	7.98	$\frac{T_{\text{cl}}}{2} + (18.23 \pm 1) j^{-(1.1 \pm 0.017)}$	0.00021
0.25	$\infty$	$(8.48 \pm 0.08) + (1.8 \pm 0.02) \ln(j)$	0.00019
0.3	13.78	$\frac{T_{\text{cl}}}{2} - (48.43 \pm 7) j^{-(1.26 \pm 0.046)}$	0.00299
		$\frac{T_{\text{cl}}}{2} - (2.5 \pm 0.1) e^{-(0.037 \pm 0.0014)j}$	0.00156

are the incomplete and complete elliptic integrals of the first kind. The inverse of  $F$  is the Jacobian amplitude “am,” and thus we gain [51]

$$\begin{aligned} \theta &= \text{am}(h_f t | (4h_f)^{-2}) \quad \text{for } 1 < 4h_f, \\ \phi &= \frac{\pi}{2} - \text{am}\left(\frac{1}{4} t \left| (4h_f)^2 \right.\right) \quad \text{for } 4h_f < 1. \end{aligned} \quad (17)$$

Once we have one of the angles, then the other one comes from (14). In the case of  $4h_f = 1$ , one can directly get

$$\theta = -\frac{\pi}{2} + 2 \arctan(e^{\frac{t}{4}}) = \frac{\pi}{2} - \phi \quad (18)$$

from (11) by exploiting (14).

By putting the angles from (17) and (18) in (10), we draw the trajectories of  $s_{\text{cl}}(t)$  for different  $h_f$  in Fig. 3. The vector  $s_{\text{cl}}(t)$  takes the half-time period from the starting point  $(0, 0, 1)$  to the turning point, where  $\theta$  goes from 0 to  $\pi$  in the case of  $1 < 4h_f$  and  $\phi$  goes from  $\frac{\pi}{2}$  to 0 in the case of  $4h_f < 1$ . Hence, using (15) and (16), one can express the time period  $T_{\text{cl}}$  and the dynamical order parameter  $m_{\text{cl}} := \frac{1}{T_{\text{cl}}} \int_0^{T_{\text{cl}}} z dt$  as [47,60]

$$\begin{aligned} T_{\text{cl}} &= \begin{cases} \frac{4}{h_f} K((4h_f)^{-2}) & \text{for } 1 < 4h_f, \\ 8K((4h_f)^2) & \text{for } 4h_f < 1, \end{cases} \\ m_{\text{cl}} &= \begin{cases} 0 & \text{for } 1 < 4h_f, \\ \frac{4\pi}{T_{\text{cl}}} & \text{for } 4h_f < 1. \end{cases} \end{aligned} \quad (19)$$

The plots for  $T_{\text{cl}}$  and  $m_{\text{cl}}$  are given in [52,60] and Fig. 5.

Taking  $m_{\text{cl}}$ , the DPT-I is described in [47,51,60,77]: for  $h_{\text{in}} = 0$ , the dynamical ordered ( $m_{\text{cl}} \neq 0$ ) and disordered ( $m_{\text{cl}} = 0$ ) phases occur when  $h_f \in [0, \frac{1}{4}]$  and  $h_f > \frac{1}{4}$ , respectively. Hence, in the case of  $h_{\text{in}} = 0$ ,  $h_f^{\text{dy}} = \frac{1}{4}$  is the *dynamical* critical point for the DPT-I and also for the DPT-II [51,60,77] that we will discuss in the next subsection.

Now, we present our contribution for this section where we show how the exact time period  $T$  goes to  $T_{\text{cl}}$  as we increase the system size  $N = 2j$ . Unlike the classical vector  $s_{\text{cl}}(t)$ , motion of the exact quantum mean vector  $s(t)$  [defined

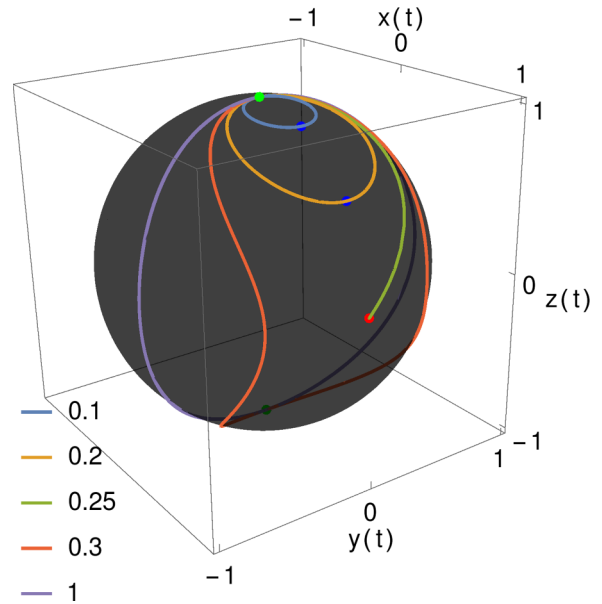


FIG. 3. Classical trajectories on the unit sphere [52,55–57,62,77,78]. Trajectories of  $s_{\text{cl}} = (x, y, z)$  of (10) are highlighted in separate colors, on the black unit sphere, for different magnitudes of  $h_f = 0.1, \dots, 1$ . All the paths start from the green point  $(0, 0, 1)$  towards the positive  $y$  direction, that is,  $(\theta_{\text{in}}, \phi_{\text{in}}) = (0, \frac{\pi}{2})$ . The blue points  $[4h_f, 0, \sqrt{1 - (4h_f)^2}]$  are the turning points for  $h_f < \frac{1}{4}$ . Whereas, the green point  $(0, 0, -1)$  is the turning point for all  $\frac{1}{4} < h_f$ . In the case of  $h_f = \frac{1}{4}$ ,  $s_{\text{cl}}$  takes infinite time to reach the red point  $(1, 0, 0)$ , and it never returns.

in (10)] is not perfectly periodic when  $N$  is finite as exhibited in Fig. 4. There one can notice that  $s$  closely follows  $s_{\text{cl}}$  in the beginning for a short time. The time interval over which the quantum evolution matches with its classical limit increases with  $N$  [52]. So, by looking at Fig. 4, we define the time  $\frac{T}{2}$  when the  $z$  component of  $s$  reaches its first minimum value that corresponds to the turning point of a classical trajectory in Fig. 3. In this way, we numerically obtain  $\frac{T}{2}$  for different  $j$  values and exhibit the data in the bottom-right plot in Fig. 4.

By employing the least-squares method from Appendix E, we get the best-fit function  $g(j)$  for the data  $\{\frac{T_j}{2}\}$  associated with  $h_f$ . For distinct  $h_f$ , the functions  $g$  are placed in Table I and exhibited in Fig. 4. The fitted functions reveal that  $T$  diverges logarithmically at the critical point  $h_f = \frac{1}{4}$  and converges to  $T_{\text{cl}}$  otherwise. In the table and figure, one can also notice that  $g(j)$  changes its behavior from a convex to a concave function as we increase  $h_f$ . To visualize it clearly we also present  $\frac{T}{2}$  as a function of  $j$  in the figure for  $h_f = 0.245$ , where  $\frac{T}{2}$  has both the convex and concave parts.

The time period  $T$  diverges when we take both the limits  $j \rightarrow \infty$  and  $4h_f \rightarrow 1$ . *Case 1:* One can take first  $j \rightarrow \infty$ . Then, the time period will be  $T_{\text{cl}}$  of (19) and the left-hand limit

$$\lim_{4h_f \rightarrow 1^-} K((4h_f)^2) = \lim_{4h_f \rightarrow 1^-} \ln\left(\frac{4}{\sqrt{1 - (4h_f)^2}}\right) \quad (20)$$

reveals the logarithm divergence with respect to the Hamiltonian parameter as in the case of a simple pendulum as reported in [52,53] and in other mean-field models [42–44,46,48,49].

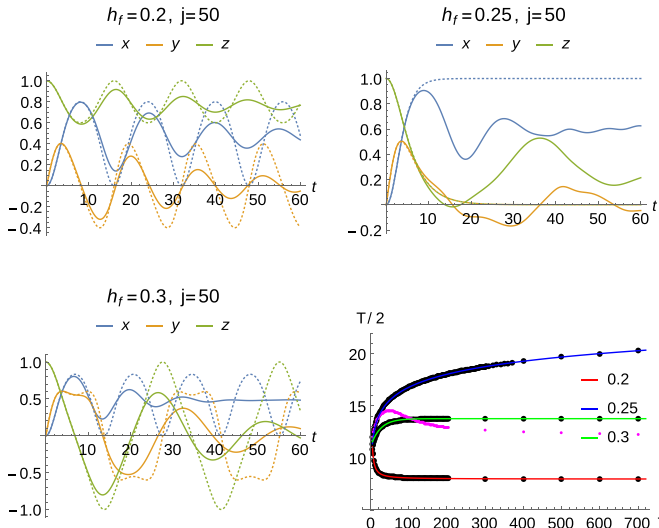


FIG. 4. Spin components versus time and the half-time period versus system size. In the first three panels, we display the components of  $\mathbf{s} = (x, y, z)$  with the solid and of  $\mathbf{s}_{\text{cl}}$  with the dotted curves for  $h_f = 0.2, 0.25$ , and  $0.3$ . The mean vector  $\mathbf{s}$  is computed numerically for  $j = 50$ , and  $\mathbf{s}_{\text{cl}}$  is acquired from (10), (17), and (18). The amplitude of oscillations does not change with time  $t$  in the dotted curves that correspond to the classical trajectories in Fig. 3. In the bottom-right plot, for  $h_f = 0.2, 0.25$ , and  $0.3$ ,  $\frac{T}{2}$  for different  $j$  values are represented by the black points. A curve passing through a sequence of black points depicts the associated best-fit function  $g(j)$  listed in Table I. The dots in magenta color show  $\frac{T}{2}$  for  $h_f = 0.245$ .

Equation (20) is borrowed from [93]. The right-hand limit  $4h_f \rightarrow 1^+$  on  $K((4h_f)^{-2})$  will deliver the same outcome. *Case 2:* One can fix first  $4h_f = 1$  and then compute the exact  $T$  for different system sizes and observe the logarithm divergence with respect to  $j$  as exhibited in Fig. 4 and Table I.

Now we demonstrate how one can take both the limits together. For all  $0 \leq 4h_f \leq 1$ , the turning point is  $(\sin \theta_{\text{tp}}, 0, \cos \theta_{\text{tp}}) = (4h_f, 0, \sqrt{1 - (4h_f)^2})$ . Suppose we increase  $h_f$  and  $j$  by maintaining a relation, say,  $\frac{1}{j^\kappa} = \frac{\pi}{2} - \theta_{\text{tp}} =: \epsilon$ , where  $\kappa > 0$ . Then, the limit  $j \rightarrow \infty$  will also serve the purpose of  $4h_f \rightarrow 1^-$ . Moreover, we gain

$$\lim_{4h_f \rightarrow 1^-} \frac{T_{\text{cl}}}{2} = \lim_{\epsilon \rightarrow 0} 4 \ln \left( \frac{4}{\sin \epsilon} \right) = \lim_{j \rightarrow \infty} 4\kappa \ln j + 4 \ln 4 \quad (21)$$

by exploiting (19), (20), and  $\sin \epsilon \approx \epsilon$ . If we take  $\epsilon := \frac{1}{\alpha j^\kappa}$  with  $\alpha > 0$ , then we can find out the values of  $\kappa$  and  $\alpha$  for which  $\frac{T_{\text{cl}}}{2}$  of (21) matches with  $g(j)$  given in Table I for  $4h_f = 1$ .

In fact, one can get an equation similar to the first one in (21) from (18) as follows. Taking the  $z$  component of  $\mathbf{s}_{\text{cl}}$  as per (18), we have the quadratic equation  $\cos \theta = \frac{2\varpi}{1+\varpi^2}$ , where  $\varpi = \exp(t/4)$ . Solving this equation for  $\varpi$  and then for  $t$  provides

$$t = 4 \ln \left( \frac{1 + \sin \theta}{\cos \theta} \right) \approx 4 \ln \left( \frac{2}{\sin \epsilon} \right), \quad (22)$$

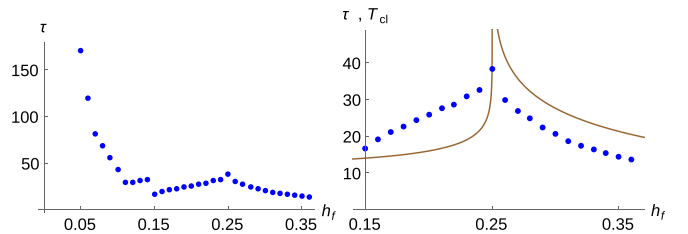


FIG. 5. First critical time versus final field strength. Taking  $j = 100$ , we plot the first critical time  $\tau$  (blue points) with respect to the field's strength  $h_f = 0.05, \dots, 0.36$ . Experimentally, a similar plot is obtained in [62] for  $1 < 4h_f$ . The right plot is a part of the left plot. For comparison, we place the brown curves that represent the classical time period given in (19).

where  $\varepsilon := \frac{\pi}{2} - \theta \approx 0$  measure how close the associated point on the classical trajectory is from the destination point  $(1, 0, 0)$ , which is shown in red color in Fig. 3.

## 2. DPT-II

Now, we consider the DPT-II. Let us recall that  $h_{\text{in}} = 0$ ,  $|\psi_{\text{in}}\rangle = |j\rangle_z$ ,  $h_{\text{in}} < h_f$ , and the Loschmidt rate function  $r(t)$  from (13). In the FCIM, there will always be kinks in  $r(t)$  at the so-called critical times [60, 75]. In the paper we only focus on the first critical time, when the *first* kink, discontinuity in  $r$ , appears, denoted by  $\tau$ . In this section, our main results are presented in Table II and Figs. 5–7. They essentially tell that, similar to  $T$  in the previous subsection, the sequence  $\tau_j$  converges to a value when  $4h_f \neq 1$ , and diverges logarithmically with the system size at the dynamical phase transition point  $4h_f = 1$ .

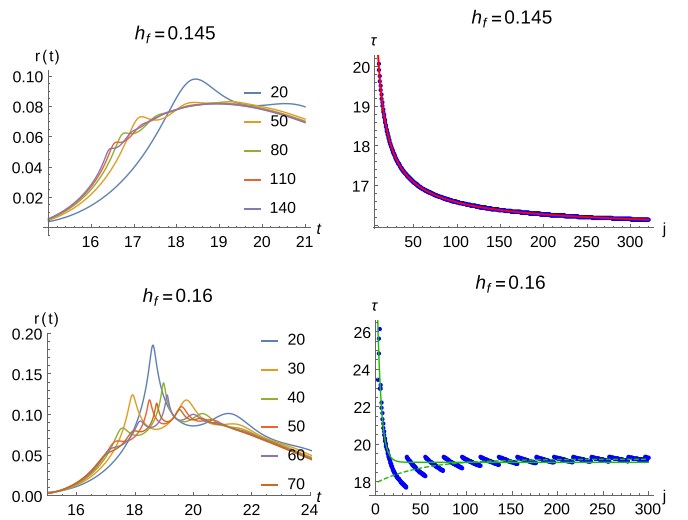


FIG. 6. The rate versus time and the first critical time versus system size. In all the plots  $h_{\text{in}} = 0$ , and the value of  $h_f$  is written at the top of each picture. In the left column, we present  $r(t)$  in distinct colors for different  $j$  values. In the right column, the first critical times  $\tau_j$  are depicted by the blue dots, and the red and green curves represent the best-fit functions  $g(j)$  of the form  $a + b j^c$  (power law) and  $a + b e^{c j}$  (exponential), respectively. The continuous and dotted green curves express the corresponding convex and concave functions. All the  $g$  functions with their  $h_f$  are recorded in Table II.

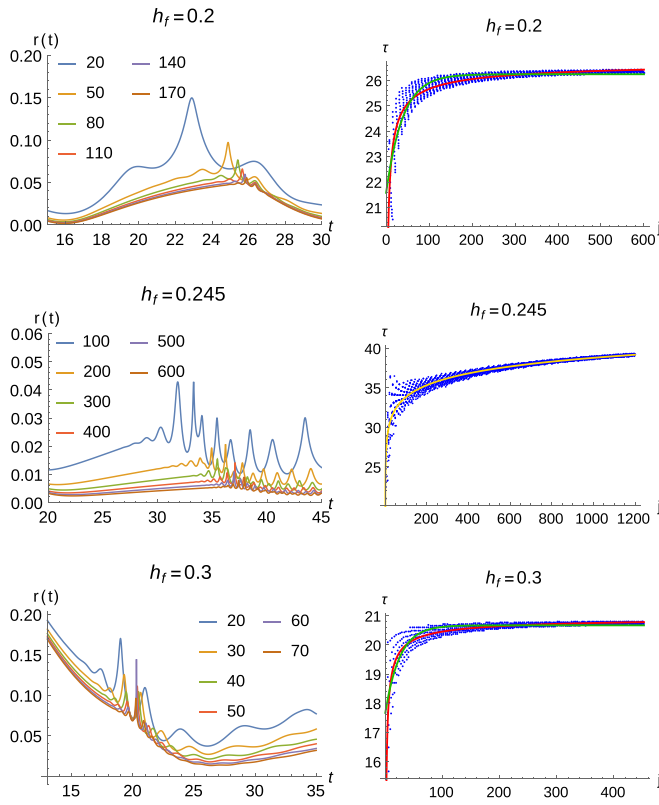


FIG. 7. The rate versus time and the first critical time versus system size. In the same fashion, this figure presents the items of Fig. 6 for the other values of  $h_f$ . The fitted curve in yellow color stands for the logarithmic function given in Table II for  $h_f = 0.245$ . Like before, the red and green fitted curves represent functions from the power-law and exponential families.

We have numerically computed the derivative using

$$\dot{r} \approx \frac{-r(t+2\varsigma) + 8r(t+\varsigma) - 8r(t-\varsigma) + r(t-2\varsigma)}{12\varsigma} \quad (23)$$

on a set of points in an appropriate time interval and obtain  $\tau$  where the absolute difference  $|\dot{r}(t+\varsigma) - \dot{r}(t)|$  is maximum. Thus, the obtained  $\tau$  are plotted in Figs. 5–7, 11, and 12.

In Fig. 5, we present  $\tau$  versus  $h_f$  plot for a fixed system size, which summarizes the behavior  $r(t)$  described through Fig. 19 in Appendix F. When  $h_f = 0.05$  is close to  $h_{in} = 0$ , the ground state  $|\psi_{in}\rangle$  does not change much for a long time, and hence the first cusp appears on the 14th peak of  $r(t)$ . When  $h_f = 0.06$ , the cusp emerges on the 10th peak, which shows a rapid decline in  $\tau$  with a small increase in  $h_f$ . A small jump in  $\tau$  around  $h_f = 0.15$  is because the first kink shifts from the third to second peak as  $h_f$  moves from 0.14 to 0.15. A similar shift happens around  $h_f = 0.1$  in Fig. 5. If we focus on  $h_f \in [0.15, 0.35]$  in the figure, then we observe  $\tau$  and  $T_{cl}$  of (19) exhibit a similar behavior: both grow with  $h_f$ , reach a peak at the dynamical phase transition point, and then they decrease.

Now we discuss how  $\tau$  varies with  $j$  for a fixed  $h_f$ . Let us take Fig. 6, where we present  $r(t)$  and  $\tau$  for different  $j$  and for  $h_f = 0.145, 0.16$  separately. In the case of  $h_f = 0.145$ , one can observe a cusp at  $r(t)$  gets sharper and sharper

TABLE II. The best-fit functions for the first critical time. For  $h_{in} = 0$ , the best-fit functions  $g(j)$  for  $\tau_j$  are recorded here with their “errors” defined in Appendix E. In the case of  $h_f = 0.2, 0.3$ , two different functions have almost the same error, so we put both of them in this table and exhibit them in Fig. 7 through red and green curves.

$h_f$	$g(j)$	error
0.05	$(167.2 \pm 0.006) + (54.2 \pm 0.3) j^{-(0.64 \pm 0.002)}$	0.0014
0.095	$(41.4 \pm 0.001) + (29.1 \pm 0.05) j^{-(0.69 \pm 0.0006)}$	0.00003
0.145	$(15.8 \pm 0.002) + (23.7 \pm 0.07) j^{-(0.75 \pm 0.001)}$	0.00002
0.16	$(19.04 \pm 0.028) + (13.6 \pm 1.5) e^{-(0.23 \pm 0.02)j}$	0.111
	$(19.2 \pm 0.03) - (1.28 \pm 0.2) e^{-(0.02 \pm 0.003)j}$	0.039
0.2	$(26.8 \pm 0.086) - (16.8 \pm 1.5) j^{-(0.577 \pm 0.037)}$	0.089
	$(26.2 \pm 0.02) - (4.7 \pm 0.2) e^{-(0.026 \pm 0.001)j}$	0.089
0.245	$(24 \pm 0.16) + (2.15 \pm 0.026) \ln(j)$	0.395
0.255	$(17.9 \pm 0.094) + (2.81 \pm 0.015) \ln(j)$	0.129
0.3	$(21 \pm 0.065) - (8.66 \pm 0.88) j^{-(0.6 \pm 0.05)}$	0.0524
	$(20.67 \pm 0.02) - (3 \pm 0.2) e^{-(0.04 \pm 0.003)j}$	0.0568
0.4	$(11.41 \pm 0.07) - (2.94 \pm 0.7) e^{-(0.241 \pm 0.07)j}$	0.127

as  $j$  increases, and it gradually shifts towards the left-hand side. Consequently, one can see the sequence  $\tau_j$  decreases monotonically and converges to a value around 16. Following the least-squares method of Appendix E, we find the best-fit function  $g(j)$  for the data  $\{\tau_j\}$  and registered it in Table II. One can see that  $g$  is a convex function, it represents a power-law convergence of  $\tau_j$  for  $h_f = 0.145$ , where the estimates of  $\tau_\infty$  and the finite-size scaling are 15.8 and 0.75, respectively. These estimates are explained in Appendix E.

Now we focus on  $r(t)$  for  $h_f = 0.16$  in Fig. 6. As we change  $j$ , the position of cusp, that is,  $\tau$  oscillates around some value, and the oscillations become smaller as  $j$  grows larger and larger. This manifests the convergence of  $\tau_j$ . If we do not (or do) ignore a first set of values in the data  $\{\tau_j\}$ , then  $g$  turns out to be a convex (concave) function. Both the convex and concave functions for  $h_f = 0.16$  are placed in Table II and plotted in Fig. 6 with the data. Both the functions belong to the exponential class, and they suggest the same  $\tau_\infty \approx 19$  but their finite-size scalings are different. For  $h_f < 0.16$ ,  $g$  are mostly convex functions, and they all are concave functions for  $h_f > 0.16$ . This change of behavior we also have observed in the case of time period  $T$  (see Fig. 4 and Table I). By the way, we get similar plots if we replace  $h_f = 0.145$  ( $h_f = 0.16$ ) by  $h_f = 0.113$  ( $h_f = 0.14$ ).

One can see in Fig. 6 for  $h_f = 0.16$  that there are multiple spikes at  $r(t)$  for each  $j$ , one of which is the sharpest measured by  $|\dot{r}(t+\varsigma) - \dot{r}(t)|$ . Recall that the time at the sharpest spike is our  $\tau_j$ . For a sequence of  $j$  values this particular spike moves a bit on the left-hand side and remains the sharpest, and then another spike becomes so. As a result, we see sudden jumps (oscillations) in  $\tau_j$  in the case  $h_f \geq 0.16$  (see Fig. 7). Due to the oscillations, the error is larger in the case of  $h_f = 0.16$  in comparison to  $h_f = 0.145$  (see Table II).

Now we move to Fig. 7 that is an extension of Fig. 6. There, in the case of  $h_f = 0.2, 0.3$ , one can observe a convergent behavior of  $r(t)$  (for more details, see Appendix H)

and thus of  $\tau$  with respect to  $j$ . There are oscillations in  $\tau$  but they get suppressed as we increase the system size  $N = 2j$ . Whereas, at the dynamical phase transition point  $h_f = 0.25$ , large and fast oscillations in  $r(t)$  pertain for a long time, and thus it becomes difficult to assign  $\tau$ . So, we pick the values  $h_f = 0.245, 0.255$  close to the transition point and obtain the data  $\{\tau_j\}$ . For each of these values, the best-fit functions  $g$  are in Table II that suggests the *logarithmic divergence* of  $\tau_j$  with respect to  $j$  at the dynamical critical point. The same type of divergence we have reported for the time period  $T_j$  in the previous subsection. For  $h_f = 0.2, 0.3$ , and  $0.4$ , the best-fit functions for the data  $\{\tau_j\}$  are placed in Table II and plotted in Fig. 7.

### B. Initially all spins are up in the $x$ direction

Throughout this section, we fix  $h_{in} \rightarrow \infty$ , and thus  $|\psi_{in}\rangle = |\frac{\pi}{2}, 0\rangle = |j\rangle_x$  is the exact ground state of Hamiltonian (1) as per (3). Like Sec. III A, let us focus on the DPT-I and DPT-II sequentially.

#### I. DPT-I

A power-law divergence of the time period in (26), (27), Fig. 9, and Table III and a power-law decay of the dynamical order parameter in (29) are our main contributions in this section. Here the energy conservation (12) becomes

$$4h_f = (\cos \theta)^2 + 4h_f \sin \theta \cos \phi, \quad (24)$$

which always has  $(\theta, \phi) = (\frac{\pi}{2}, 0)$  as its solution. For all  $h_f \geq \frac{1}{2}$ , it is the only possible solution. However, for every  $h_f \in [0, \frac{1}{2}]$ , Eq. (24) has more than one solution.

In this paragraph, we borrow some results from [9]. Since  $(\theta_{in}, \phi_{in}) = (\frac{\pi}{2}, 0)$  is a fixed point of classical equations of motion (11), we take  $\theta_{in} = \frac{\pi}{2} - \epsilon$  to start the motion. Picking  $\epsilon = 10^{-3}$ , we plot the classical trajectories of  $s_{cl}$  of (10) for different  $h_f \in (0, \frac{1}{2})$ . Each trajectory represents a periodic motion of the unit vector  $s_{cl}$ . Corresponding to the (approximate) turning point  $s_{cl} = [4h_f - 1, 0, \sqrt{1 - (4h_f - 1)^2}]$  displayed in blue or green color in Fig. 8, we have  $\theta_{tp} = \arcsin |4h_f - 1|$  and  $\phi_{tp} = 0$  or  $\pi$ . From  $\theta_{tp}$  to  $\theta_{in}$ , the angle  $\theta$  takes the half-time period, hence, we get

$$\begin{aligned} \frac{T_{cl}}{2} &= 4 \int_{\theta_{tp}}^{\theta_{in}} \frac{\sin \theta d\theta}{\cos \theta \sqrt{(\cos \theta_{tp})^2 - (\cos \theta)^2}} \\ &= -4 \frac{1}{\cos \theta_{tp}} \ln \left( \frac{\frac{\cos \theta_{in}}{\cos \theta_{tp}}}{1 + \sqrt{1 - \left( \frac{\cos \theta_{in}}{\cos \theta_{tp}} \right)^2}} \right) \\ &\approx -4 \frac{1}{\cos \theta_{tp}} \ln \left( \frac{\epsilon}{\cos \theta_{tp} + \sqrt{(\cos \theta_{tp})^2 - \epsilon^2}} \right). \end{aligned} \quad (25)$$

The first equation in (25) is derived from the first equation in (11) with the help of (24). After the integration, we reach the second expression. Then, after applying  $\cos \theta_{in} = \sin \epsilon \approx \epsilon$ , we arrive at the last expression in (25), which is slightly different than the one achieved in [9]. For all  $0 \leq h_f \leq \frac{1}{2}$ , the time period  $T_{cl}$  diverges as  $\epsilon \rightarrow 0$ , and there are two kinds of divergences.

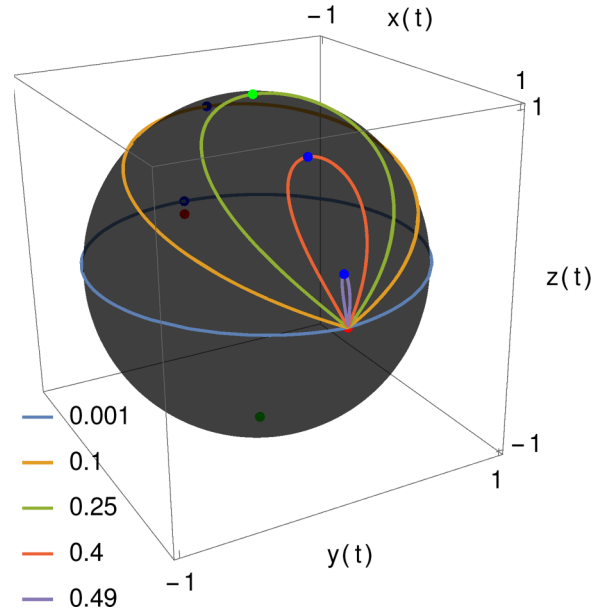


FIG. 8. Classical trajectories on the unit sphere. Trajectories of  $s_{cl}$  are illustrated in different colors for  $h_f = 0.001, \dots, 0.49$ . They are obtained by numerically solving equations of motion (11) with the initial condition  $(\theta_{in}, \phi_{in}) = (\frac{\pi}{2} - \epsilon, 0)$ , where  $\epsilon = 10^{-3}$ . Since  $\epsilon > 0$ , the motion will be on the upper hemisphere. Every trajectory starts from the red point, that is approximately  $(1, 0, 0)$ , towards the negative  $y$  direction and follows energy conservation (24).

*Logarithmic divergence:* When  $0 < h_f < \frac{1}{2}$ , then  $\cos \theta_{tp}$  is nonzero, and the divergence is due to  $\ln(\epsilon)$  only, as reported in [9]. For example, let us take  $4h_f = 1$ , then we get  $\cos \theta_{tp} = 1$  and  $\frac{T_{cl}}{2} \approx -4 \ln(\frac{\epsilon}{2})$ , which is similar to the results presented in (21) and (22).

*Power-law divergence:* When  $h_f \rightarrow 0$  or  $\frac{1}{2}$ , then we also have a divergence due to  $\cos \theta_{tp} \rightarrow 0$ . To combine both the limits, we propose an association  $\theta_{tp} := \frac{\pi}{2} - 2\epsilon$ . By the association,  $\epsilon \rightarrow 0$  will automatically execute the limit  $h_f \rightarrow 0$  or  $\frac{1}{2}$ . Moreover, we get  $\cos \theta_{tp} = \sin(2\epsilon) \approx 2\epsilon$  and then

$$\frac{T_{cl}}{2} \approx \frac{2 \ln(2 + \sqrt{3})}{\epsilon} = 2 \ln(2 + \sqrt{3}) j^\kappa, \quad (26)$$

where  $\kappa > 0$ . The first and last expressions in (26) come from (25) and the relation  $\epsilon := \frac{1}{j^\kappa}$ , which is proposed in the text around (21).

The above analysis suggests logarithmic and power-law divergences of  $T_{cl}$ . To check this for different system sizes, we numerically computed the exact  $\frac{T}{2}$ , when the  $x$  component of  $s$  of (10) reaches its first minimum value. For distinct  $h_f$ , we present  $\frac{T_j}{2}$  versus  $j$  plots in Fig. 9 with their best-fit functions  $g(j)$ , which are listed in Table III. The functions  $g$  are acquired by following the least-squares method of Appendix E. In Appendix G, for  $h_f = 0$  and  $j \geq 1$ , we have analytically shown

$$\frac{T}{2} = \tau = \begin{cases} 4\pi j & \text{when } j \text{ is an integer,} \\ 2\pi j & \text{when } j \text{ is a half-integer} \end{cases} \quad (27)$$

(see also the top-left plot in Fig. 9). With Fig. 9, Table III, and (27), one can deduce that the time period indeed follows

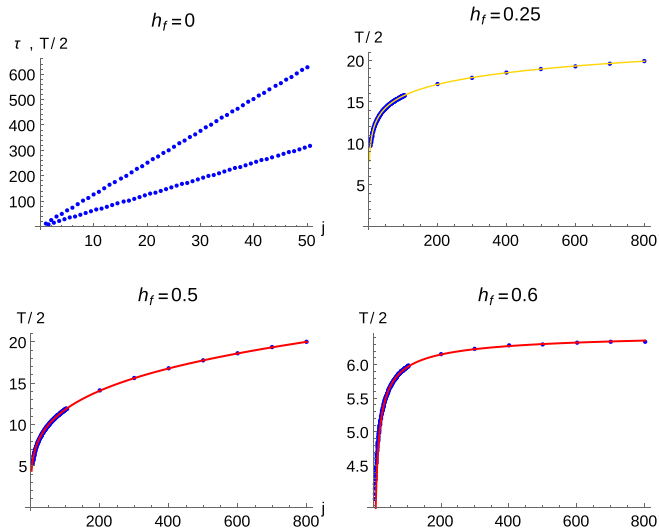


FIG. 9. The half-time period versus system size. In each plot, the associated  $h_f$  value is placed at the top, and  $\frac{T_j}{2}$  are depicted through the blue points for a sequence of  $j$  values. The red (power-law) and yellow (logarithmic) curves portray the  $g$  functions listed in Table III that best fit the (data) blue points. In the case of  $h_f = 0$ , the two straight lines of points follow (27).

a power-law divergence when  $h_f$  is 0 or  $\frac{1}{2}$  and follows a logarithmic divergence when  $h_f$  is in the middle.

In Fig. 9 and Table III, we also present  $\frac{T_j}{2}$  with its  $g$  for  $h_f = 0.6$ , which reveals a convergent behavior of  $T_j$  against  $j$ . Such convergent behavior exists for all  $h_f > \frac{1}{2}$ . For a higher  $h_f$ ,  $T_j$  converges faster and to a smaller value.

Before moving to the next subsection, let us note that  $|\psi_{in}\rangle = |j\rangle_x$  and therefore  $|\psi(t)\rangle$  are eigenkets of the spin-flip operator  $X$  due to its commutation with the Hamiltonian given in (A1). As a result, we have  $\langle\psi(t)|J_z|\psi(t)\rangle = 0$  for all  $t \geq 0$ . So, rather than taking the  $z$  component of  $s$  of (10), we have taken above its  $x$  component as it is related through the energy conservation to the dynamical order parameter  $m' := \lim_{\zeta \rightarrow \infty} \int_0^\zeta \langle(\frac{d\theta}{dt})^2\rangle dt$  considered in [9].

Like (25), one can obtain

$$\begin{aligned} m_{cl} &:= \frac{2}{T_{cl}} \int_{\frac{T_{cl}}{2}}^{T_{cl}} \cos \theta \, dt \\ &= \frac{8}{T_{cl}} \int_{\theta_{tp}}^{\theta_{in}} \frac{\sin \theta \, d\theta}{\sqrt{(\cos \theta_{tp})^2 - (\cos \theta)^2}} \\ &= -\frac{8}{T_{cl}} \cos \theta_{tp} \left[ \arcsin \left( \frac{\cos \theta_{in}}{\cos \theta_{tp}} \right) - \frac{\pi}{2} \right], \\ m'_{cl} &:= \frac{2}{T_{cl}} \int_{\frac{T_{cl}}{2}}^{T_{cl}} (\cos \theta)^2 \, dt \\ &= \frac{8}{T_{cl}} \cos \theta_{tp} \sqrt{1 - \left( \frac{\cos \theta_{in}}{\cos \theta_{tp}} \right)^2} \end{aligned} \quad (28)$$

by taking  $\theta_{in} = \frac{\pi}{2} - \epsilon$ , where  $\epsilon > 0$ . A slightly different expression of  $m'_{cl}$  is achieved in [9], where it is shown that  $m'$  reaches its peak value at  $4h_f = 1$ , and the value goes to zero as a multiple of  $\frac{1}{\ln(j)}$  in the classical limit  $j \rightarrow \infty$ . Provided

TABLE III. The best-fit functions for the half-time period. For  $h_{in} \rightarrow \infty$ , the best-fit functions  $g(j)$  for  $\frac{T_j}{2}$  are recorded here with the associated error like Table I. In fact,  $h_f = 0.25$  corresponds to the same situation here as well as in Table I. The time period  $T_{cl}$  comes from (25) and (26) after taking the limit  $\epsilon \rightarrow 0$ .

$h_f$	$\frac{T_{cl}}{2}$	$g(j)$	error
0.25	$\infty$	$(6.44 \pm 0.072) + (2.02 \pm 0.012) \ln(j)$	0.00003
0.5	$\infty$	$(3.69 \pm 0.005) j^{(0.253 \pm 0.0002)}$	0.00002
0.6		$(6.5 \pm 0.01) - (9.2 \pm 0.2) j^{-(0.61 \pm 0.009)}$	0.00002

$h_f$  does not approach to 0 or  $\frac{1}{2}$  (that is,  $\cos \theta_{tp} \neq 0$ ), we have  $m_{cl} \approx \frac{4\pi}{T_{cl}} \cos \theta_{tp}$  and  $m'_{cl} \approx \frac{8}{T_{cl}} \cos \theta_{tp}$  for a sufficiently small  $\epsilon$ . Particularly at  $4h_f = 1$ , we have  $\cos \theta_{tp} = 1$ , hence, we get  $m_{cl} \approx \frac{4\pi}{T_{cl}}$  same as (19) and  $m'_{cl} \approx \frac{8}{T_{cl}}$ . And, due to the logarithmic divergence of  $T_{cl}$  discussed above,  $m$  also goes to zero as a multiple of  $\frac{1}{\ln(j)}$  in the classical limit.

In the case of  $h_f \rightarrow 0$  or  $\frac{1}{2}$ , we run an analysis similar to (26) for  $m_{cl}$  as well as  $m'_{cl}$  by taking  $\theta_{tr} = \frac{\pi}{2} - 2\epsilon$  and obtain

$$\begin{aligned} m_{cl} &\approx \frac{4\pi}{3 \ln(2 + \sqrt{3})} \epsilon^2 = \frac{4\pi}{3 \ln(2 + \sqrt{3})} j^{-2\kappa}, \\ m'_{cl} &\approx \frac{2\sqrt{3}}{\ln(2 + \sqrt{3})} \epsilon^2 = \frac{2\sqrt{3}}{\ln(2 + \sqrt{3})} j^{-2\kappa} \end{aligned} \quad (29)$$

from (28). Result (29) suggests a *power-law decay* of  $m$  and  $m'$  with the system size when  $h_f$  is very near to 0 or  $\frac{1}{2}$ .

Strictly speaking, we have the energy gap  $\Delta \neq 0$  when  $0 < h_{in}, j < \infty$  as discussed in Sec. II, and  $\langle J_z \rangle = 0 = m$  as  $|\psi_{in}\rangle = |e_0\rangle$  is an eigenket of  $X$ . However, for a finite  $j$ , when the gap becomes almost zero in the ferromagnetic phase ( $\theta_0 < \frac{\pi}{2}$ ), the ground-state vector can be taken as one of the mean-field kets, that is,  $|\psi_{in}\rangle = |\theta_0\rangle$  as per (3). Then, we get  $\langle J_z \rangle \neq 0 \neq m$  and the above results of  $m$  can be realized for a finite  $j$  and  $2h_{in} < 1$ .

For  $h_{in} \rightarrow \infty$  and  $h_f = 0$ , the exact  $m = 0$  and  $m' = \frac{1}{2j}$  for all  $j$  [see (G5)]. The dynamical order parameters  $m_{cl}$  of (28) and  $m'$  are plotted in Fig. 11 and Ref. [9], respectively.

## 2. DPT-II

Figures 11, 12, and 22 as well as Tables IV and V hold our main results for this section. They basically present how the critical time  $\tau$  and the rate  $r(\tau)$  perform with growing number  $N = 2j$  of spins. Here  $\tau$  diverges logarithmically or with a power law like  $T$  in the previous subsection, and  $r(\tau)$  goes to zero provided  $h_f$  is nonzero.

Now let us recall the rate  $r(t)$  from (13) to study the DPT-II in the case where all the spins are initially polarized in the  $x$  direction,  $|\psi_{in}\rangle = |j\rangle_x$ . Keeping the system size fixed, we plot  $r(t)$  for different  $h_f$  in the top row in Fig. 10. There one can observe that the first cusp appears at the first peak of  $r(t)$  when  $h_f \in [0, \frac{1}{2}]$  and no cusp appears when  $\frac{1}{2} < h_f$ . This identifies the regular ( $h_f \leq \frac{1}{2}$ ) and trivial ( $\frac{1}{2} < h_f$ ) phases [60,75]. As we increase the final field's strength from 0 to  $\frac{1}{2}$ , the first kink shifts towards the left-hand side, which implies that the first critical time  $\tau$  decreases with  $h_f$ . This is presented in Fig. 11, where one can notice that both  $\tau$  and the time period of (25) follow similar behavior with  $h_f$  except around  $\frac{1}{2}$ .

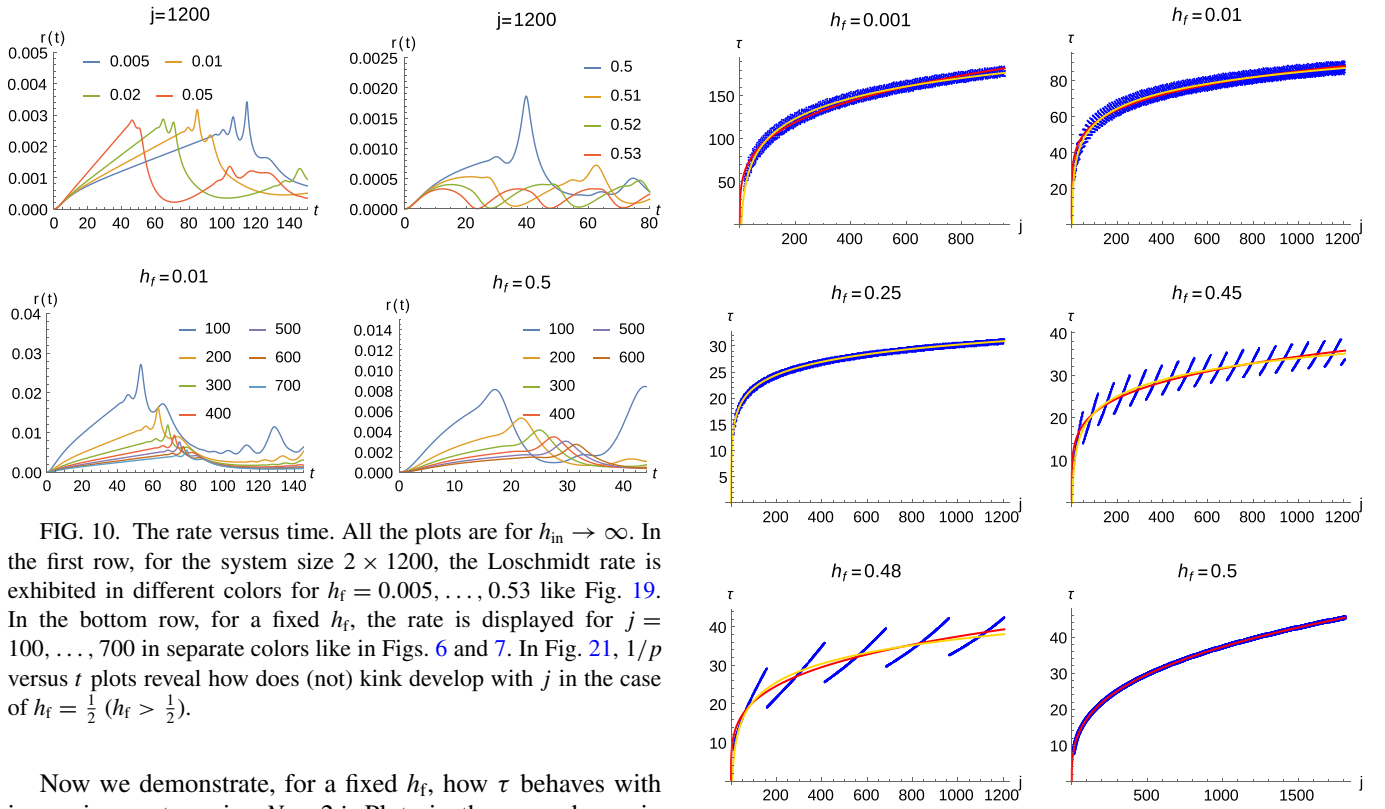


FIG. 10. The rate versus time. All the plots are for  $h_{\text{in}} \rightarrow \infty$ . In the first row, for the system size  $2 \times 1200$ , the Loschmidt rate is exhibited in different colors for  $h_f = 0.005, \dots, 0.53$  like Fig. 19. In the bottom row, for a fixed  $h_f$ , the rate is displayed for  $j = 100, \dots, 700$  in separate colors like in Figs. 6 and 7. In Fig. 21,  $1/p$  versus  $t$  plots reveal how does (not) kink develop with  $j$  in the case of  $h_f = \frac{1}{2}$  ( $h_f > \frac{1}{2}$ ).

Now we demonstrate, for a fixed  $h_f$ , how  $\tau$  behaves with increasing system size  $N = 2j$ . Plots in the second row in Fig. 10 reveal that (i) the first kink moves towards the right-hand side, which indicates that  $\tau_j$  grows with  $j$  towards infinity. (ii) The height of the kink (or peak) decreases towards zero as  $j$  goes to infinity provided  $h_f \neq 0$ . Observations (i) and (ii) are justified by the exact data  $\{\tau_j\}$  and  $\{Nr(\tau_j)\}$  plotted in Figs. 12 and 22, respectively. Table V provides the best-fit functions for the data  $\{Nr(\tau_j)\}$ , which suggests a power-law decay of  $r(\tau_j)$  to zero as  $j$  goes to infinity.

Now let us focus on observation (i). The best-fit function  $g(j)$  for the data  $\{\tau_j\}$  are displayed in Fig. 12 and listed in Table IV with their  $h_f$  values. There one can see that,

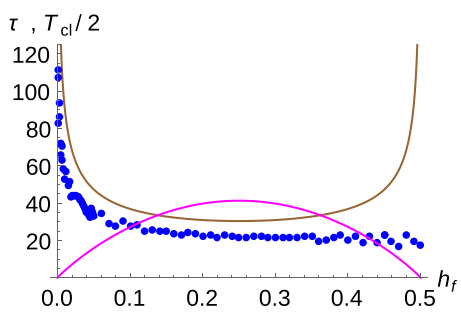


FIG. 11. First critical time versus final field strength. Having  $j = 100$  and  $|\psi_{\text{in}}\rangle = |j\rangle_x$ , here we present the first critical time  $\tau$  for  $h_f = 0.0005, \dots, 0.5$ , which suggests  $\tau \rightarrow \infty$  as  $h_f \rightarrow 0$  even for a finite system size. The brown curve represents [the last expression of (25) for  $\epsilon = 10^{-3}$ ] the half-time period as a function of the field strength  $h_f$  like Fig. 5. All the blue points and the whole brown curve will go to infinity in the limits  $j \rightarrow \infty$  (see Fig. 12) and  $\epsilon \rightarrow 0$ , respectively. The magenta curve portrays  $100 \times m_{\text{cl}}$ , where  $\epsilon = 10^{-3}$  and the dynamical order parameter  $m_{\text{cl}}$  is given in (28). In the limit  $\epsilon \rightarrow 0$ , we have  $m_{\text{cl}} \rightarrow 0$  for every  $h_f$ .

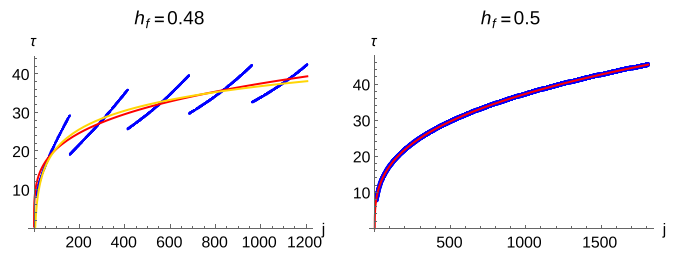


FIG. 12. First critical time versus system size. Similar to Figs. 6 and 7, all these plots are for  $h_{\text{in}} \rightarrow \infty$ , that is,  $|\psi_{\text{in}}\rangle = |j\rangle_x$ . The blue points represent the exact data  $\{\tau_j\}$  procured for the  $h_f$  values stated at the top of each plot. Like Sec. III A 2, here the data show oscillations of  $\tau$  with respect to  $j$  except in the case of  $h_f = 0.5$ . The red and yellow curves exhibit the power law and logarithmic best-fit functions  $g$ , respectively, from Table IV. As we go from  $h_f = 0.001$  to  $h_f = 0.5$ , the color of curves is changing from red to yellow to red, which reflects the change of functional form of  $g$  in Table IV. The plots for  $h_f = 0.001, 0.01, 0.45, 0.48$  carry both the red and yellow curves.

when  $h_f = 0.001$  is close to 0 or  $h_f = \frac{1}{2}$ ,  $g(j)$  represents a *power-law divergence* of the critical time with the system size. Whereas,  $g(j)$  suggests a *logarithmic divergence* when  $h_f = \frac{1}{4}$  is in-between zero and one-half. The same behavior is exhibited by the time period  $T$  in Sec. III B 1.

#### IV. SUMMARY

We have exhibited that the time period  $T$  in DPT-I and the first critical time  $\tau$  in DPT-II exhibit similar converging or diverging behaviors with respect to the system size, in the fully connected quantum Ising model. Initially if all the spins are in the  $z$  direction with respect to Hamiltonian (1), both  $T$  and  $\tau$  diverge *logarithmically* with the number  $N$  of spins at the dynamical phase transition point  $h_f = \frac{1}{4}$ . If all the spins are in the  $x$  direction at the beginning, then both  $T$  and  $\tau$  diverge over the whole interval  $[0, \frac{1}{2}]$  where the final field strength  $h_f$  lies. At the end points of the interval, the divergence is through a *power law*, and it is logarithmic in the middle. In the case of convergence, we have reported estimates for the finite-size scaling and converged value for  $T$  as well as for  $\tau$ .

TABLE IV. The best-fit functions for the first critical time. For  $h_{\text{in}} \rightarrow \infty$ , the best-fit functions  $g$  for  $\tau$  are recorded here with the associated error like Table II. The data  $\{\tau_j\}$  with their  $g(j)$  are plotted in Fig. 12. Here as we go from top to bottom the functional form (divergent nature) of  $g$  changes from power law to logarithmic to power law. We have witnessed the same behavior in Table III in the case of  $T$ . For  $h_f = 0$ ,  $\tau$  is stated in (27) and exhibited in the top-left plot of Fig. 9. Two different functions have almost the same errors in the case of  $h_f \in \{0.01, 0.45, 0.48\}$ , so we place both of them in the table. Since  $\tau$  values are bigger when  $h_f = 0.001$  (see Figs. 11 and 12), error has the highest value in the table. Whereas, in the case of  $h_f = 0.48$ , the higher error is due to the large oscillations in the data  $\{\tau_j\}$  (see Fig. 12).

$h_f$	$g(j)$	error
0.001	$(28.5 \pm 0.5) j^{(0.27 \pm 0.003)}$	26.98
	$-(57 \pm 1.5) + (34.1 \pm 0.25) \ln(j)$	22.2
0.01	$(24.6 \pm 0.3) j^{(0.18 \pm 0.002)}$	7.58
	$-(2.08 \pm 0.69) + (12.6 \pm 0.11) \ln(j)$	6.21
0.25	$(5.44 \pm 0.1) + (3.59 \pm 0.02) \ln(j)$	0.132
0.45	$-(4.55 \pm 0.56) + (5.59 \pm 0.09) \ln(j)$	4.04
	$(8.1 \pm 0.2) j^{(0.21 \pm 0.004)}$	4.09
0.48	$-(11.2 \pm 0.8) + (6.95 \pm 0.1) \ln(j)$	8.01
	$(6.2 \pm 0.2) j^{(0.26 \pm 0.005)}$	7.69
0.5	$(3.77 \pm 0.001) j^{(0.332 \pm 0.00004)}$	0.00058

Using a mean-field analysis, we have obtained the time period  $T_{\text{cl}}$  and the order parameters  $m_{\text{cl}}$  and  $m'_{\text{cl}}$  as functions of the Hamiltonian parameter, and then obtained them as functions of the system size to analytically justify their converging or diverging behavior at the transition points. However, for the initial field strength  $h_{\text{in}} \rightarrow \infty$  and  $h_f = 0$ , we have achieved  $T$ ,  $\tau$ ,  $m$ , and  $m'$  as functions of  $N$  through a direct calculation. We have also reported that the Loschmidt rate at the critical time  $r(\tau)$  goes to zero in the case of  $h_{\text{in}} \rightarrow \infty$  and to a nonzero value for  $h_{\text{in}} = 0$ , with power laws as we grow the system size  $N$ . It will be interesting to run a similar investigation for the DPTs in other mean-field models studied in [42–44,46,48,49].

The analysis of the dynamical properties of the model is preceded, in this paper, by a brief presentation of its certain equilibrium properties. There, for a finite system, we have demonstrated that the approximate energy eigenkets  $|\chi\rangle$  and the associated exact energy eigenkets  $|e\rangle$  show a large overlap, provided we do not go too close to the equilibrium phase transition point. In addition, we have captured the energy gap and entanglement properties of the ground and first excited states through  $|\chi\rangle$ . We have found a good agreement between approximate and exact results in the case of energy gap and geometric entanglement (an  $N$ -body entanglement quantifier). Whereas, the concurrence (a two-body entanglement measure) showed a good match only in the paramagnetic phase. In the case of  $|\chi\rangle$ , we have obtained analytical formulas for the energy gap, concurrence, and geometric entanglement. Furthermore, we have exhibited that, at the equilibrium critical point, the geometric entanglement and concurrence of the first excited state  $|e_1\rangle$  also grow with power laws as we increase  $N$ .

## ACKNOWLEDGMENTS

We acknowledge support from the Department of Science and Technology, Government of India through the QuEST grant (Grant No. DST/ICPS/QUEST/Theme-3/2019/120). For the numerical computations, we are grateful to the cluster computing facility at the Harish-Chandra Research Institute, India. We are grateful to J. Larson for his comments.

## APPENDIX A: BETTER APPROXIMATION OF GROUND AND FIRST EXCITED STATES

In this Appendix, first, we present our motivations for choosing  $|\chi\rangle$  of (4) rather than the two coherent kets  $|\theta_0\rangle$  and  $|\pi - \theta_0\rangle$  that are mentioned around (3). Then, we show, through the numerical data in Figs. 13–15, that  $|\chi\rangle$  indeed provides better approximation of  $|e\rangle$  than the coherent kets.

First let us note that the Hamiltonian of (1) commutes with  $\mathbf{S}^2 = \mathbf{S} \cdot \mathbf{S}$ , where  $\mathbf{S} = (S_x, S_y, S_z)$ , and with the spin-flip operator  $X := \otimes_{i=1}^N \sigma_i^x$  [30]:

$$[H, \mathbf{S}^2] = 0 = [H, X]. \quad (\text{A1})$$

At the zero temperature, for a ferromagnetic coupling  $\Gamma > 0$ , the ground state-vector  $|e_0\rangle$  lies in the eigenspace

$$\mathcal{S} = \text{span}(\mathcal{B}_z), \quad \mathcal{B}_z = \{|m\rangle_z\}_{m=-j}^j \quad (\text{A2})$$

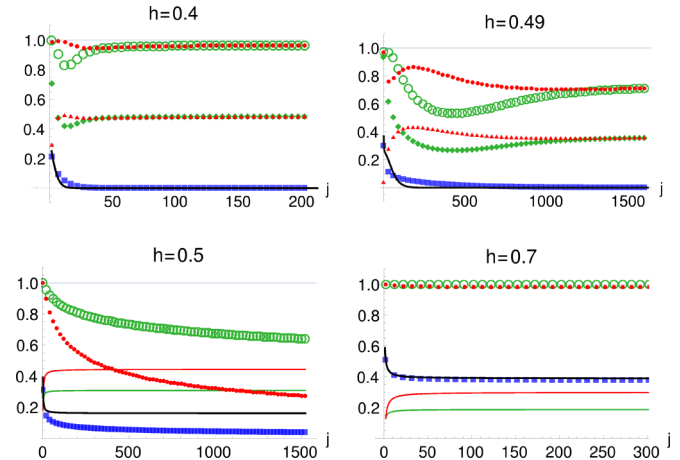


FIG. 13. Overlap versus system size. The top- and bottom-row plots are for  $2h < 1$  (ferromagnetic) and  $1 \leq 2h$  (paramagnetic), correspondingly. The green circles ( $\circ$ ) denote  $|\langle \chi_{+}|e_0\rangle|^2$  and  $|\langle \chi_0|e_0\rangle|^2$  in the top- and bottom-row plots, respectively. Likewise, the red points ( $\bullet$ ) exhibit  $|\langle \chi_-|e_1\rangle|^2$  in the top plots and  $|\langle \chi_0|e_1\rangle|^2$  in the bottom plots as functions of  $j$ . In the top panels for  $h = 0.4, 0.49$ , the green diamonds ( $\blacklozenge$ ) and red triangles ( $\blacktriangle$ ) express  $|\langle \theta_0|e_0\rangle|^2$  and  $|\langle \theta_0|e_1\rangle|^2$ , correspondingly. In all the pictures, the blue squares ( $\blacksquare$ ) represent the exact energy gap  $\Delta$  between the ground and first excited states, and the black curves represent the approximate energy gap:  $\Delta_{\text{app}}$  from (A6) for  $2h < 1$  and  $\varepsilon_1 - \varepsilon_0$  from (B3) and (B4) for  $1 \leq 2h$ . The green and red curves in the bottom-row plots illustrate  $\frac{\mu_0}{2}$  and  $\frac{\mu_1}{2}$  [given in (B3) and (B4)], respectively. In Fig. 14, more such plots are given for  $h$  close to the transition point.

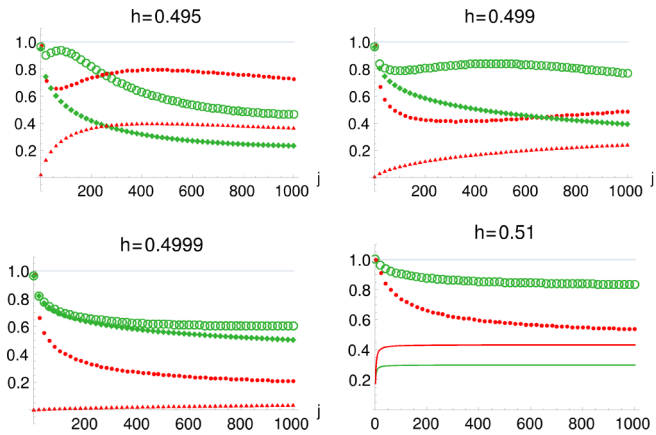


FIG. 14. Overlap versus system size. It is an extension of Fig. 13. Here the  $h$  values are taken near the equilibrium phase transition point  $h = 0.5$ .

of  $S^2$  spanned by the Dicke kets [94]. The Dicke and spin coherent [86] kets can be explicitly written as

$$\begin{aligned} |m\rangle_z &= \frac{1}{\sqrt{\binom{2j}{j+m}}} (|\uparrow_z\rangle^{\otimes j+m} |\downarrow_z\rangle^{\otimes j-m} + \text{per}), \\ |\theta, \phi\rangle &= \left( \cos \frac{\theta}{2} |\uparrow_z\rangle + \sin \frac{\theta}{2} e^{i\phi} |\downarrow_z\rangle \right)^{\otimes 2j} \\ &= \sum_{m=-j}^j \binom{2j}{j+m}^{\frac{1}{2}} \left( \cos \frac{\theta}{2} \right)^{j+m} \left( \sin \frac{\theta}{2} e^{i\phi} \right)^{j-m} |m\rangle_z, \end{aligned} \quad (\text{A3})$$

respectively, where  $|\uparrow_z, \downarrow_z\rangle$  are the  $+1, -1$  eigenvalue kets of the single-spin Pauli operator  $\sigma^z$ , and “per” denotes all possible permutations. Now we first take the case  $0 < 2h < 1$ . The two coherent kets are the zeroth-order mean-field approximations of  $|e_0\rangle$  [30,85]. To see how well the mean-field approximation works for  $j < \infty$ , we plot the overlaps  $|\langle\theta_0|e_0\rangle|^2$  as well as  $|\langle\theta_0|e_1\rangle|^2$  as functions of  $j$  for fixed  $h$  values in Figs. 13 and 14, and as functions of  $h$  for a fixed  $j$  value in Fig. 15. The overlap measures the closeness of two quantum states, and it is unity (zero) if and only if the two states are the same (mutually orthogonal).

One can observe the following: (i) both the overlaps are not unity but close to one-half if we neglect small- $j$  values in the case of  $h = 0.4$  in Fig. 13 (see also Fig. 15). The

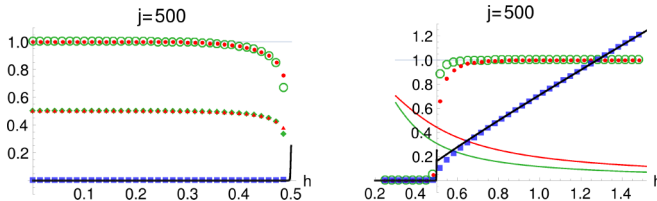


FIG. 15. Overlap versus external field strength. The left- and right-hand-side pictures are for  $2h < 1$  (ferromagnetic) and  $1 \leq 2h$  (paramagnetic), respectively. Here the only difference with respect to Fig. 13 is that the system size  $2j$  is fixed and the same quantities are presented as functions of the field strength  $h$ .

same is true if we pick the other coherent ket  $|\pi - \theta_0\rangle$ . (ii) As the ground and first excited states are nondegenerate for a finite  $j$  and  $0 < h$  [7,8,30], they must be eigenstates of the spin-flip operator  $X$  according to the second commutator in (A1). With  $X|\theta_0\rangle = |\pi - \theta_0\rangle$ , one can realize that neither of the two mean-field coherent kets is an eigenket of  $X$  but  $|\chi_{\pm}\rangle$  of (4) are [5]. Moreover, the two coherent kets are neither the same nor mutually orthogonal because  $\langle\theta_0|\pi - \theta_0\rangle = (\sin\theta_0)^N$ , whereas  $\langle\chi_+|\chi_-\rangle = 0$ . The operator  $X$  owns only two distinct eigenvalues  $\pm 1$ , and  $\mathcal{E}_{\pm}$  are the associated eigenspaces. (iii) One can directly check that the exact energy eigenkets  $|e_0\rangle \in \mathcal{E}_+$  and  $|e_1\rangle \in \mathcal{E}_-$ .

Based on the three observations,  $|\chi_+\rangle$  seems to be a better approximate of  $|e_0\rangle$  than the mean-field kets for a finite  $N$  and  $0 < 2h < 1$ . It is also suggested in [5]. To test this hypothesis, we plot the overlaps  $|\langle\chi_+|e_0\rangle|^2$  and  $|\langle\chi_-|e_1\rangle|^2$  as functions of  $j$  in Fig. 13, and one can show that

$$\begin{aligned} \sqrt{\frac{1 + (2h)^{2j}}{2}} \langle\chi_+|e_0\rangle &= \langle\theta_0|e_0\rangle = \langle\pi - \theta_0|e_0\rangle, \\ \sqrt{\frac{1 - (2h)^{2j}}{2}} \langle\chi_-|e_1\rangle &= \langle\theta_0|e_1\rangle = -\langle\pi - \theta_0|e_1\rangle \end{aligned} \quad (\text{A4})$$

as a result of observation (iii). Since  $|\langle\chi|e\rangle| \geq |\langle\theta_0|e\rangle|$  due to (A4), indeed  $|\chi\rangle$  is a better approximate of  $|e\rangle$  as exhibited in Figs. 13–15.

In Fig. 13, one can also notice that both the overlaps  $|\langle\chi_+|e_0\rangle|^2$  and  $|\langle\chi_-|e_1\rangle|^2$  are close to one once we neglect the first few values of  $j$  in the case of  $h = 0.4$ . The overlaps show the same behavior for  $h = 0.49$  but we may need to ignore more  $j$  values to see them getting closer to one. For a large system size (see Fig. 15) the two overlaps stay close to one as long as we do not go very near to the phase transition point (see also Fig. 14). So, in the ferromagnetic case, once we neglect small  $j$  values, then we can make the approximations  $|e_0\rangle \approx |\chi_+\rangle$  and  $|e_1\rangle \approx |\chi_-\rangle$  for  $j < \infty$  in the sense that  $|\langle\psi|\psi'\rangle|^2 \approx 1$  implies  $|\psi'\rangle\langle\psi'| \approx |\psi\rangle\langle\psi|$ .

Before moving to the paramagnetic case  $1 \leq 2h$ , let us record that  $\mathcal{E}_+ \oplus \mathcal{E}_- = \mathcal{S}$  of (A2). Furthermore, taking the eigenkets of  $S_x$  such that  $(S_x - m)|m\rangle_x = 0$ , we can write

$$\begin{aligned} \mathcal{E}_+ &= \text{span}\{|j - 2k\rangle_x | k = 0, 1, \dots, \lceil j - \frac{1}{2} \rceil\}, \\ \mathcal{E}_- &= \text{span}\{|j - (2k + 1)\rangle_x | k = 0, 1, \dots, \lfloor j - \frac{1}{2} \rfloor\}, \end{aligned} \quad (\text{A5})$$

where  $\lceil \dots \rceil$  and  $\lfloor \dots \rfloor$  are the ceiling and floor functions. One can differentiate the eigenkets of  $S_z$  in (A2) from the eigenkets of  $S_x$  in (A5) by their subscripts.

Now we pick the paramagnetic case, where the mean-field ket  $|\frac{\pi}{2}\rangle = |j\rangle_x \in \mathcal{E}_+$  as per (3), (A3), and (A5). Comparing with (2), when  $k < \infty$ , every  $|j - k\rangle_x$  gives the same minimum energy  $\lim_{j \rightarrow \infty} \frac{x(j-k)|H|j-k\rangle_x}{j} = -h$  in the thermodynamic limit. So, for  $1 \leq 2h$ , we choose  $|\chi_{0,1}\rangle \in \mathcal{E}_{+,-}$  in (4), whose parameters  $\mu_{0,1}$  are obtained in Appendix B that provide the minimum energies  $\varepsilon_{0,1} := \langle\chi_{0,1}|H|\chi_{0,1}\rangle$  over the two-dimensional subspaces of  $\mathcal{E}_{+,-}$  where  $|\chi_{0,1}\rangle$  live. In Fig. 13, for  $h = 0.5, 0.7$ , we display the overlaps  $|\langle\chi_{0,1}|e_{0,1}\rangle|^2$  and  $\mu_{0,1}$ . There one can perceive that  $\mu_0 \neq 0$  for both the  $h$

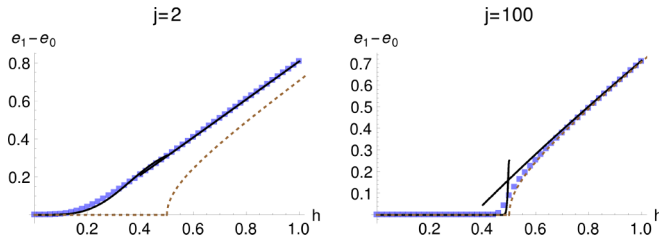


FIG. 16. Energy gap versus external field strength. The exact energy difference  $\Delta$  is illustrated by the blue squares ( $\blacksquare$ ) for two different system sizes (see also Figs. 13 and 15). The black curves represent  $\Delta_{\text{app}}$  described in the text around (A6). The brown dotted curve depicts 0 for  $0 \leq 2h < 1$  and  $\sqrt{h(h-1/2)}$  for  $1 \leq 2h$  [8].

values, hence,  $|\chi_0\rangle$  is a better approximation of the ground-state vector than the mean-field ket  $|j\rangle_x$  for a finite  $j$ . This completes our justification for (5). By the way, for  $j \gg 1$ , even better approximation of the paramagnetic ground state is presented in [21].

On the right-hand side in Fig. 15, we present the values of  $|\langle\chi_{0,1}|e_{0,1}\rangle|^2$  and  $\mu_{0,1}$  as functions of the field strength. One can witness that both  $\mu_{0,1}$  decrease as  $h$  rises beyond the transition point. When the field strength is very large, then obviously  $|e_k\rangle \approx |j-k\rangle_x$  for  $k = 0, 1, \dots$ , and thus we reach  $\mu_{0,1} \approx 0$ .

### Energy gap

Here we compare the actual energy gap  $\Delta := e_1 - e_0$  with the approximate gap  $\Delta_{\text{app}}$  calculated using  $|\chi\rangle$  from (4). Let us first consider  $|\chi_{\pm}\rangle$  that corresponds to  $0 < 2h < 1$ . In the span of  $\{|\chi_{\pm}\rangle\}$ ,  $|\chi_+\rangle$  and  $|\chi_-\rangle$  are the only kets that provide the maximum overlaps with the exact ground- and first-excited-state vectors, respectively. Since  $\mathcal{E}_+$  and  $\mathcal{E}_-$  of (A5) are mutually orthogonal invariant subspaces of Hamiltonian (1),  $H$  is diagonal in the orthonormal basis  $\{|\chi_{\pm}\rangle\}$  of a two-dimensional subspace, and

$$\begin{aligned} \Delta_{\text{app}} &:= \langle\chi_-|H|\chi_-\rangle - \langle\chi_+|H|\chi_+\rangle \\ &= \frac{(N+1)(\cos\theta_0)^2(\sin\theta_0)^N}{4[1-(\sin\theta_0)^{2N}]} \geq 0. \end{aligned} \quad (\text{A6})$$

Expression (A6) has already been reported in [5].

Now we take  $|\chi_{0,1}\rangle$  that corresponds to  $1 \leq 2h$ , where  $\Delta_{\text{app}} = \varepsilon_1 - \varepsilon_0$  is specified by  $\varepsilon_{0,1}$  in (B3) and (B4). In Fig. 16, we display the actual as well as approximate energy gap and observe a good match for all  $h$  values except near the critical point. The exact energy gap follows the power law, viz.,  $\Delta \sim j^{-\frac{1}{3}}$  at the phase transition point  $2h = 1$  [7,8,85], which we can not get from (A6) because  $\lim_{\theta_0 \rightarrow \frac{\pi}{2}} \Delta_{\text{app}} = \frac{1}{4}$  for  $N \gg 1$ . Nevertheless, one can witness through (A6) that the gap closes exponentially fast in the ferromagnetic phase with  $N$  due to the factor  $(\sin\theta_0)^N$  [85].

In the paramagnetic phase, we have  $\varepsilon_1 - \varepsilon_0 \approx h - \frac{1}{4}$  in the thermodynamic limit according to (B5). In Fig. 16, we also display a result  $\sqrt{h(h-1/2)}$  for  $1 \leq 2h$  from [8], which is exact for the limit  $j \rightarrow \infty$ . One can see that  $\sqrt{h(h-1/2)} \approx h - \frac{1}{4}$  for a large  $h$ , hence, it matches with our  $\Delta_{\text{app}}$ .

### APPENDIX B: ENERGY MINIMIZATION IN THE PARAMAGNETIC PHASE

Here the task is to find  $|\chi\rangle$  [see (4)] (in the two-dimensional space spanned by  $\mathbf{B}_x := \{|m\rangle_x, |m'\rangle_x\}$ , where  $j - 3 \leq m' = m - 2$ ) that provides the minimum energy  $\varepsilon := \langle\chi|H|\chi\rangle$ . To complete the task, we restrict Hamiltonian (1) onto  $\text{span}(\mathbf{B}_x)$ , then the restricted Hamiltonian in the basis  $\mathbf{B}_x$  is represented by

$$H|_{\mathbf{B}_x} \equiv \begin{pmatrix} {}_x\langle m|H|m\rangle_x & {}_x\langle m|H|m'\rangle_x \\ {}_x\langle m'|H|m\rangle_x & {}_x\langle m'|H|m'\rangle_x \end{pmatrix} =: -\underbrace{\begin{pmatrix} a & b \\ b & c \end{pmatrix}}_M, \quad (\text{B1})$$

where  $a, c \in \mathbb{R}$  and  $b \geq 0$  for all  $j \geq 1$ . The eigenvalues and eigenvectors of  $M$  are

$$\begin{aligned} \zeta_{\pm} &= \frac{(a+c) \pm \text{Disc}}{2} \quad \text{and} \\ |\zeta_{\pm}\rangle &= \sqrt{\frac{1 \pm \cos\mu}{2}} |m\rangle_x \pm \sqrt{\frac{1 \mp \cos\mu}{2}} |m'\rangle_x, \quad \text{where} \\ \cos\mu &= \frac{a-c}{\text{Disc}}, \quad \sin\mu = \frac{2b}{\text{Disc}}, \quad \text{and} \\ \text{Disc} &= \sqrt{(a-c)^2 + (2b)^2}. \end{aligned} \quad (\text{B2})$$

Clearly,  $|\chi\rangle = |\zeta_+\rangle \in \text{span}(\mathbf{B}_x)$  will provide the minimum energy  $\varepsilon = -\zeta_+ < 0$ , and  $\mu \in [0, \pi]$ . If one wants even better approximation of the ground and first excited states, then she can repeat the above method by taking a larger set, say,  $\mathbf{B}_x = \{|m\rangle_x, |m'\rangle_x, |m''\rangle_x\}$  where  $m'' + 4 = m' + 2 = m = j - 1$ .

In the case of  $|\chi_0\rangle$  of (4), we have  $m = j$  and get

$$\begin{aligned} \mu_0 &= \arccos\left(\frac{4h-1+\frac{1}{j}}{2\text{Disc}}\right), \\ \varepsilon_0 &= -\frac{1}{2}\left(\frac{6j-4}{8j} + 2h(j-1) + \text{Disc}\right), \\ \text{Disc} &= \frac{1}{2}\sqrt{\left(4h-1+\frac{1}{j}\right)^2 + \frac{j(2j-1)}{(2j)^2}}. \end{aligned} \quad (\text{B3})$$

In the case of  $|\chi_1\rangle$ ,  $m = j - 1$ , and we obtain

$$\begin{aligned} \mu_1 &= \arccos\left(\frac{4h-1+\frac{2}{j}}{2\text{Disc}}\right), \\ \varepsilon_1 &= -\frac{1}{2}\left(\frac{10j-10}{8j} + 2h(j-2) + \text{Disc}\right), \\ \text{Disc} &= \frac{1}{2}\sqrt{\left(4h-1+\frac{2}{j}\right)^2 + \frac{3(j-1)(2j-1)}{(2j)^2}}. \end{aligned} \quad (\text{B4})$$

In the classical limit, we get

$$\begin{aligned} \mu_0 &= \arccos\left(\frac{4h-1}{\sqrt{(4h-1)^2 + \frac{1}{2}}}\right), \\ \mu_1 &= \arccos\left(\frac{4h-1}{\sqrt{(4h-1)^2 + \frac{3}{2}}}\right), \end{aligned}$$

$$\begin{aligned} \lim_{j \rightarrow \infty} (\varepsilon_1 - \varepsilon_0) &= h - \frac{1}{4} + \frac{1}{4} \left( \sqrt{(4h-1)^2 + \frac{1}{2}} \right. \\ &\quad \left. - \sqrt{(4h-1)^2 + \frac{3}{2}} \right) \\ &\approx h - \frac{1}{4} \quad \text{for a large } h. \end{aligned} \quad (B5)$$

APPENDIX C: CONCURRENCE OF  $|\chi\rangle\langle\chi|$ 

We have  $N$ -body symmetric quantum states such as  $|\chi\rangle\langle\chi|$  and  $|e\rangle\langle e|$  in Sec. II, and here we are interested in their bipartite quantum entanglement, as quantified by the concurrence [11,12].

It is shown in [89] that, for every symmetric state, the two-body reduced density matrix can be expressed as

$$\rho = \begin{pmatrix} a_+ & d_+^* & d_+^* & b^* \\ d_+ & c & c & d_-^* \\ d_+ & c & c & d_- \\ b & d_- & d_- & a_- \end{pmatrix}, \quad \text{where}$$

$$a_{\pm} = \frac{1}{4} \left( 1 \pm \frac{4 \langle J_z \rangle}{N} + \frac{4 \langle J_z^2 \rangle - N}{N^2 - N} \right),$$

$$b = \frac{\langle J_x^2 \rangle - \langle J_y^2 \rangle + i \langle [J_x, J_y]_+ \rangle}{N^2 - N},$$

$$\lambda_1 = 0, \quad \lambda_2 = (a - b)^2,$$

$$\lambda_3 = \frac{(a+b)^2 + 4(c^2 - 2d^2) + (a+b-2c)\sqrt{(a+b+2c)^2 - 16d^2}}{2},$$

$$\lambda_4 = \frac{(a+b)^2 + 4(c^2 - 2d^2) - (a+b-2c)\sqrt{(a+b+2c)^2 - 16d^2}}{2} \quad (C4)$$

of  $\rho \tilde{\rho}$  for concurrence  $C := \max\{0, \sqrt{\lambda_m} - \sum_{\lambda \neq \lambda_m} \sqrt{\lambda}\}$  [11,12]. In the case of exact ground and first-excited energy eigenkets  $|e_{0,1}\rangle$ , we exploit (C3) and (C4) to numerically compute the concurrence and present the results in Fig. 1.

In the case of  $|\chi_{\pm}\rangle\langle\chi_{\pm}|$ ,  $\theta = \theta_0$ , we get

$$\begin{aligned} a^{(\pm)} &= \frac{1 + \cos \theta^2 \pm \sin \theta^N}{4(1 \pm \sin \theta^N)}, \\ b^{(\pm)} &= \frac{\sin \theta^2 \pm (1 + \cos \theta^2) \sin \theta_0^{N-2}}{4(1 \pm \sin \theta^N)}, \\ c^{(\pm)} &= \frac{\sin \theta^2 (1 \pm \sin \theta^{N-2})}{4(1 \pm \sin \theta^N)}, \\ d^{(\pm)} &= \frac{\sin \theta (1 \pm \sin \theta^{N-2})}{4(1 \pm \sin \theta^N)}, \end{aligned} \quad (C5)$$

$$c = \frac{N^2 - 4 \langle J_z^2 \rangle}{4(N^2 - N)},$$

$$d_{\pm} = \frac{1}{2} \left( \frac{\langle J_x \rangle + i \langle J_y \rangle}{N} \pm \frac{\langle [J_x, J_z]_+ \rangle + i \langle [J_y, J_z]_+ \rangle}{N^2 - N} \right), \quad (C1)$$

and  $[A, B]_+ := AB + BA$ . The matrix in (C1) is in the basis  $\{| \uparrow_z \uparrow_z \rangle, | \uparrow_z \downarrow_z \rangle, | \downarrow_z \uparrow_z \rangle, | \downarrow_z \downarrow_z \rangle\}$ , and all the expectation values are computed with the parent  $N$ -spin state from which  $\rho$  is obtained.

Since both  $|\chi\rangle$  and  $|e\rangle$  are eigenkets of the spin-flip operator  $X$  [given in (A1)] for  $0 < h, j < \infty$ , and  $X$  anticommutes with  $J_y, J_z, J_x J_y$ , and  $J_x J_z$ , we get the zero expectation values

$$\langle J_y \rangle = \langle J_z \rangle = \langle [J_x, J_y]_+ \rangle = \langle [J_x, J_z]_+ \rangle = 0 \quad (C2)$$

from both the keys. Furthermore, as all the coefficients  ${}_z\langle m|\chi\rangle$  and  ${}_z\langle m|e\rangle$  of the two kets are real numbers in the basis  $\mathcal{B}_z$  of (A2), the matrix in (C1) will be real (that is,  $\rho = \rho^*$ ), and thus  $\langle [J_y, J_z]_+ \rangle = 0$ . So, in the case of approximate  $|\chi\rangle$  and exact  $|e\rangle$  eigenkets of Hamiltonian (1), (C1) turns into

$$\rho = \begin{pmatrix} a & d & d & b \\ d & c & c & d \\ d & c & c & d \\ b & d & d & a \end{pmatrix}, \quad \text{where}$$

$$a = \frac{1}{4} \left( 1 + \frac{4 \langle J_z^2 \rangle - N}{N^2 - N} \right), \quad b = \frac{\langle J_x^2 \rangle - \langle J_y^2 \rangle}{N^2 - N}, \quad (C3)$$

$$c = \frac{N^2 - 4 \langle J_z^2 \rangle}{4(N^2 - N)}, \quad d = \frac{\langle J_x \rangle}{2N},$$

and we get the eigenvalues

which give

$$\begin{aligned} \lambda_2 &= \frac{\cos \theta^4 (1 \mp \sin \theta^{N-2})^2}{4(1 \pm \sin \theta^N)^2}, \\ \lambda_3 &= \frac{\cos \theta^4 (1 \pm \sin \theta^{N-2})^2}{4(1 \pm \sin \theta^N)^2}, \\ \lambda_4 &= 0, \quad \text{and thus} \end{aligned}$$

$$C_{\chi_{\pm}} = \pm \sqrt{\lambda_3} \mp \sqrt{\lambda_2}. \quad (C6)$$

The concurrences  $C_{\chi_{\pm}}$  of  $|\chi_{\pm}\rangle$  are rewritten in (6) and plotted in Fig. 1.

Since the kets  $|\chi_{0,1}\rangle$  in (4) are expressed in the basis  $\mathcal{B}_x = \{|m\rangle_x\}_{m=-j}^j$ , it is easy to represent their reduced density matrix

$$\rho_x = \begin{pmatrix} v & 0 & 0 & u \\ 0 & w & w & 0 \\ 0 & w & w & 0 \\ u & 0 & 0 & v' \end{pmatrix} \quad (C7)$$

in the basis  $\{| \uparrow_x \uparrow_x \rangle, | \uparrow_x \downarrow_x \rangle, | \downarrow_x \uparrow_x \rangle, | \downarrow_x \downarrow_x \rangle\}$ . The matrices in (C3) and (C7) are related via the local unitary transformation  $\rho = H \otimes H(\rho_x)H \otimes H$ , where the Hadamard operator  $H$  interchanges the bases as  $| \uparrow_x \rangle \leftrightarrow | \uparrow_z \rangle$  and  $| \downarrow_x \rangle \leftrightarrow | \downarrow_z \rangle$ . Since  $H \otimes H$  commutes with  $\sigma_y \otimes \sigma_y$ , we get  $\rho \tilde{\rho} = H \otimes H(\rho_x \tilde{\rho}_x)H \otimes H$ , and the eigenvalues of  $\rho_x \tilde{\rho}_x$  are

$$\begin{aligned}\lambda_1 &= 0, \quad \lambda_2 = (2w)^2, \quad \lambda_3 = (\sqrt{v'v'} + u)^2, \\ \lambda_4 &= (\sqrt{v'v'} - u)^2.\end{aligned}\quad (C8)$$

In the case of  $|\chi_0\rangle$ , we get

$$\begin{aligned}v &= \left(\cos \frac{\mu_0}{2}\right)^2 + \left(\sin \frac{\mu_0}{2}\right)^2 \frac{(N-2)(N-3)}{N(N-1)} \approx 1, \\ v' &= \left(\sin \frac{\mu_0}{2}\right)^2 \frac{2}{N(N-1)} \approx \left(\sin \frac{\mu_0}{2}\right)^2 \frac{2}{N^2}, \\ u &= \sin \frac{\mu_0}{2} \cos \frac{\mu_0}{2} \sqrt{\frac{2}{N(N-1)}} \approx \sin \frac{\mu_0}{2} \cos \frac{\mu_0}{2} \frac{\sqrt{2}}{N}, \\ w &= \left(\sin \frac{\mu_0}{2}\right)^2 \frac{2(N-2)}{N(N-1)} \approx \left(\sin \frac{\mu_0}{2}\right)^2 \frac{2}{N},\end{aligned}\quad (C9)$$

where the approximation is taken under the condition  $N \gg 1$ . For  $j \geq 1$ , with (B3), (C8), and (C9), one can realize that the concurrence of  $|\chi_0\rangle$  is [89]

$$\begin{aligned}C_{\chi_0} &= 2 \max\{(u-w), 0, (w-\sqrt{v'v'})\} \quad \text{for } h \geq 0 \\ &= 2(u-w) \quad \text{for } h \geq 0.5.\end{aligned}\quad (C10)$$

In the case of  $|\chi_1\rangle$ , we attain

$$\begin{aligned}v &= \left(\cos \frac{\mu_1}{2}\right)^2 \frac{(N-2)}{N} + \left(\sin \frac{\mu_1}{2}\right)^2 \frac{(N-3)(N-4)}{N(N-1)} \approx 1, \\ v' &= \left(\sin \frac{\mu_1}{2}\right)^2 \frac{6}{N(N-1)} \approx \left(\sin \frac{\mu_1}{2}\right)^2 \frac{6}{N^2}, \\ u &= \sin \frac{\mu_1}{2} \cos \frac{\mu_1}{2} \frac{1}{N} \sqrt{\frac{6(N-2)}{N-1}} \approx \sin \frac{\mu_1}{2} \cos \frac{\mu_1}{2} \frac{\sqrt{6}}{N}, \\ w &= \left(\cos \frac{\mu_1}{2}\right)^2 \frac{1}{N} + \left(\sin \frac{\mu_1}{2}\right)^2 \frac{3(N-3)}{N(N-1)} \approx \frac{2-\cos \mu_1}{N}.\end{aligned}\quad (C11)$$

For  $j \geq 1$ , with (B4), (C8), and (C11), we discover that the concurrence of  $|\chi_1\rangle$  is

$$C_{\chi_1} = 2(w - \sqrt{v'v'}) \quad \text{for } h \geq 0. \quad (C12)$$

Concurrences (C10) and (C12) are restated in (6) and plotted in Fig. 1.

#### APPENDIX D: GEOMETRIC ENTANGLEMENT OF $|\chi\rangle\langle\chi|$

Here we provide certain results regarding the geometric entanglement of  $|\chi\rangle$  and  $|e\rangle$ . Since these kets are symmetric under the particle permutations and have real expansion coefficients in the basis  $\mathcal{B}_z$  of (A2), their closest product states will also follow these two properties. So, from (A3), we take the coherent ket  $|\theta = \vartheta, \phi = 0\rangle = |\vartheta\rangle$  with the angular variable  $\vartheta \in [0, 2\pi)$  that covers all the real symmetric product kets of  $N$  spins.

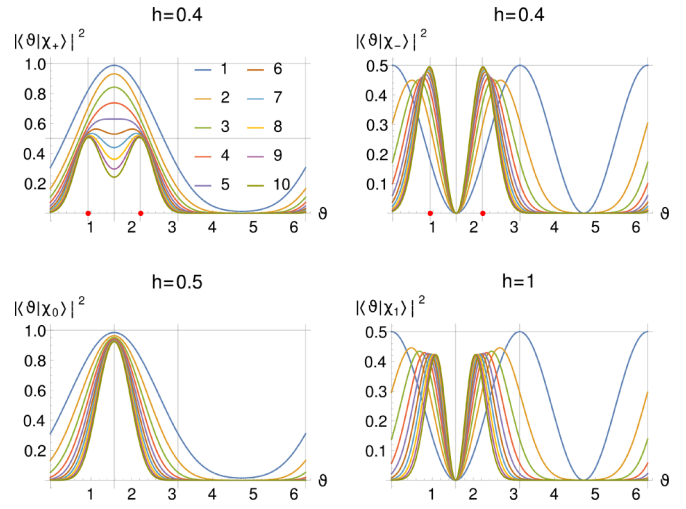


FIG. 17. Overlap between the coherent ket and approximate energy eigenkets. The absolute square of the inner products between the coherent ket  $|\vartheta\rangle$  and the approximate eigenkets  $|\chi\rangle$  is highlighted in distinct colors for  $j = 1, \dots, 10$ . In all the pictures, the color coding is the same. Graphs at the top belong to the ferromagnetic phase  $0 \leq 2h < 1$ , where the red points indicate  $\theta_0 = \arcsin(2h)$  and  $\pi - \theta_0$  that are associated with  $|\chi_{\pm}\rangle$ . Graphs at the bottom are connected to  $|\chi_{0,1}\rangle$  that are given for  $1 \leq 2h$ .

The inner products between the coherent ket  $|\vartheta\rangle$  and the approximate eigenkets  $|\chi\rangle$  of (4) are

$$\begin{aligned}\langle \vartheta | \chi_{\pm} \rangle &= \frac{\cos \left( \frac{\vartheta - \theta_0}{2} \right)^N \pm \sin \left( \frac{\vartheta + \theta_0}{2} \right)^N}{\sqrt{2[1 \pm (\sin \theta_0)^N]}}, \\ \langle \vartheta | \chi_0 \rangle &= \cos \frac{\mu_0}{2} \cos \left( \frac{\pi}{4} - \frac{\vartheta}{2} \right)^N \\ &\quad + \sin \frac{\mu_0}{2} \sqrt{\binom{N}{2}} \cos \left( \frac{\pi}{4} - \frac{\vartheta}{2} \right)^{N-2} \sin \left( \frac{\pi}{4} - \frac{\vartheta}{2} \right)^2, \\ \langle \vartheta | \chi_1 \rangle &= \cos \frac{\mu_1}{2} \sqrt{\binom{N}{1}} \cos \left( \frac{\pi}{4} - \frac{\vartheta}{2} \right)^{N-1} \sin \left( \frac{\pi}{4} - \frac{\vartheta}{2} \right) \\ &\quad + \sin \frac{\mu_1}{2} \sqrt{\binom{N}{3}} \cos \left( \frac{\pi}{4} - \frac{\vartheta}{2} \right)^{N-3} \sin \left( \frac{\pi}{4} - \frac{\vartheta}{2} \right)^3.\end{aligned}\quad (D1)$$

We plot their absolute squares as functions of  $\vartheta$  in Fig. 17 for different  $j = \frac{N}{2}$  and  $h$ . Recall the  $\theta_0$ ,  $\mu_0$ , and  $\mu_1$  are functions of  $j$  and  $h$  as per (3), (B3), and (B4), respectively. In the figure, for  $2h < 1$ , one can see that the maximum of  $|\langle \vartheta | \chi_{+} \rangle|^2$  shifts from  $\vartheta = \frac{\pi}{2}$  to  $\vartheta = \theta_0$  and  $\vartheta = \pi - \theta_0$  as  $j$  grows. On the other hand,  $|\langle \vartheta | \chi_{-} \rangle|^2$  has two peaks of the equal height, and they move from 0 and  $\pi$  to  $\theta_0$  and  $\pi - \theta_0$ , respectively, as the system size increases. So, the maximum values will be  $|\langle \theta_0 | \chi_{\pm} \rangle|^2$  for a large  $j$ , and thus we get  $G_{\chi_{\pm}}$  in (7). Closer we are to the phase transition point  $2h = 1$ , the larger  $N$  we need to achieve  $G_{\chi_{\pm}}$  in (7).

In the case of  $1 \leq 2h$ , the peak of  $|\langle \vartheta | \chi_0 \rangle|^2$  is always at  $\vartheta = \frac{\pi}{2}$  [Fig. 17], so we get  $G_0$  in (7) using (D1). Whereas  $|\langle \vartheta | \chi_1 \rangle|^2$  has two peaks of the same height, and they move from 0 and  $\pi$  towards  $\frac{\pi}{2}$  as  $j$  grows, but we have to find

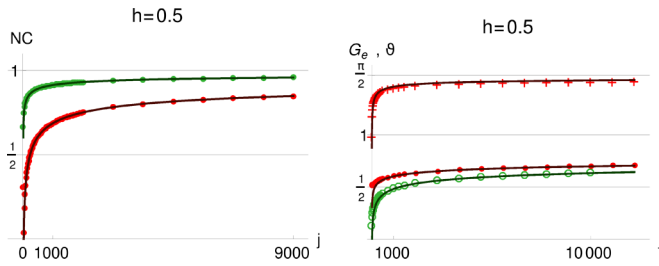


FIG. 18. Concurrence and geometric entanglement versus system size at the equilibrium phase transition point. At the phase transition point  $2h = 1$ , the exact rescaled concurrence  $NC$  and geometric entanglement  $G$  are displayed in the left and right panels, respectively. Like Figs. 1 and 2, the green and red color objects are associated with  $|e_0\rangle$  and  $|e_1\rangle$ , respectively. Red + marks represent the value of  $\vartheta$  which gives the maximum overlap  $|\langle \vartheta | e_1 \rangle|^2$ . The curves fitting the data sets are described in (8).

$\vartheta$  numerically where the maximum of  $|\langle \vartheta | \chi_1 \rangle|^2$  occurs. Figure 18 shows the concurrence and geometric entanglement of the exact energy eigenstates at the equilibrium phase transition point. The figure is discussed in the main text around (8).

#### APPENDIX E: LEAST-SQUARES METHOD

In Sec. III, we have studied the time period  $T$  and the first critical time  $\tau$  as functions of  $j$ , which are obtained numerically. As a result, we get a list of values  $f_j$  for a set of  $j$ . Here  $f$  represents  $T$  or  $\tau$ . To find a function  $g(j)$  that best fits the data  $\{f_j\}$ , we adopt the least-squares method [95,96], which is briefly described now.

We consider three kinds of functions:

$$\begin{aligned} v(c, j) &\in \{j^c, e^{cj}, \ln(j)\}, \quad \text{with} \\ g(j) &:= a + b v(c, j), \quad \text{and} \\ \chi^2 &= \sum_j \left( \frac{f_j - g(j)}{\sigma_j} \right)^2. \end{aligned} \quad (\text{E1})$$

Since the data points  $f_j$  do not have error bars (measurement errors), we take all their standard deviations  $\sigma_j$  to be equal. Then, by minimizing  $\chi^2$  over the real parameters in  $\{a, b, c\}$  in case of the three  $v$ 's, we obtain the *least-squares (maximum likelihood) estimate*  $\{a, b, c\}$  and the function  $v(c, j)$  that provide the best fit  $g(j) = a + b v(c, j)$  for a given data set.

The best-fit function gives the least possible error,

$$\text{error} = \sqrt{\frac{1}{\Omega - \Omega'} \sum_j [f_j - g(j)]^2}, \quad (\text{E2})$$

where  $\Omega$  and  $\Omega'$  are, respectively, the number of the data points and fitting parameters. Now we show how we compute the error bars (confidence intervals) for the parameters. Suppose  $g$  is a function of  $\Omega' = 3$  parameters in  $\{a, b, c\}$ , and we compute the  $\Omega \times \Omega'$  matrix

$$V := \begin{pmatrix} \vdots & \vdots & \vdots \\ \frac{\partial g(j)}{\partial a} & \frac{\partial g(j)}{\partial b} & \frac{\partial g(j)}{\partial c} \\ \vdots & \vdots & \vdots \end{pmatrix}. \quad (\text{E3})$$

When  $g$  is a linear function of the parameters, then  $V$  will be independent of the parameters.  $V$ , however, will depend on the parameters, if  $g$  is a nonlinear function of them.

In the case of a linear function, the standard errors of the parameter estimators are

$$\begin{aligned} \text{se}(a) &= \text{error} \sqrt{[(V^\top V)^{-1}]_{11}}, \\ \text{se}(b) &= \text{error} \sqrt{[(V^\top V)^{-1}]_{22}}, \\ \text{se}(c) &= \text{error} \sqrt{[(V^\top V)^{-1}]_{33}}, \end{aligned} \quad (\text{E4})$$

where  $[(V^\top V)^{-1}]_{ii}$  is the  $i$ th diagonal entry in the matrix  $(V^\top V)^{-1}$ , and  $\top$  denotes the transpose. A  $1 - \alpha$  marginal confidence interval for the parameter  $a$  is given by

$$a \pm \text{se}(a) t\left(\Omega - \Omega', 1 - \frac{\alpha}{2}\right), \quad (\text{E5})$$

where  $t(\Omega - \Omega', 1 - \frac{\alpha}{2})$  is the  $1 - \frac{\alpha}{2}$  quantile of the Student's  $t$  distribution with  $\Omega - \Omega'$  degrees of freedom [95]. Like in (E5), we can get the confidence intervals for the other parameters also.

When  $g$  is a nonlinear function of the parameters, then we first obtain the maximum likelihood estimate  $\{a, b, c\}$ , around which  $g$  will be *approximately* linear. So we evaluate  $V$  at those  $\{a, b, c\}$  and then the approximate confidence intervals through (E4) and (E5). In all the tables in the paper, we report estimated parameters as per (E5) with the 95% confidence level (that is, with  $\alpha = 0.05$ ) and the corresponding “error” defined in (E2).

*Diverging case:* If the sequence  $f_j$  appears diverging to  $\infty$ , we fix  $a = 0$  for  $a + bj^c$  and  $a + be^{cj}$ , and then follow the above procedure. Moreover, we cannot pick  $c < 0$  in (E1). In this case, through the best-fit function, we report the nature of divergence: power law  $j^c$ , exponential  $e^{cj}$ , or logarithmic  $a + b \ln(j)$  (for example, see Tables III and IV).

*Converging case:* As  $j$  grows, if the sequence  $f_j$  seems converging to a known value  $f_\infty := \lim_{j \rightarrow \infty} f_j$  then we take  $a = f_\infty$  (for instance, see Table I), otherwise the obtained  $a$  will be our estimate for  $f_\infty$  (for example, see Table II). Here we cannot take  $v$  to be  $\ln(j)$  or  $c > 0$  in (E1). If the best-fit function turns out  $g(j) = a + b j^c$  then  $c \leq 0$  will give an estimate of the log-log finite-size scaling because  $\ln|g(j) - a| = \ln|b| + c \ln(j)$ . If the best-fit function comes out  $g(j) = a + b e^{cj}$  then  $c \leq 0$  will provide an estimate of the log-linear scaling as  $\ln|g(j) - a| = \ln|b| + c j$ .

#### APPENDIX F: RATE VERSUS TIME FOR $h_{\text{in}} = 0$

In Fig. 19, for  $h_{\text{in}} = 0$ , we display  $r(t)$  for different  $h_f$ , which are studied in [60,61,75,76,78]. In Fig. 19(a), one can observe that the first kinks, marked by the arrows, appear at the fourth, third, and second peaks of  $r(t)$  when  $h_f = 0.1$ , 0.115, and 0.145, respectively. It implies that  $\tau$  decreases from  $\infty$  to a value around 16 as  $h_f$  rises from 0 to 0.145. For all  $h_f \in [0.145, \frac{1}{4}]$ , the first kink emerges at the second peak as shown in Figs. 19(a)–19(c). However, the kink moves at a later time as  $h_f$  grows. It reveals that  $\tau$  rises from 16 as we increase the final field's strength from 0.145 to  $\frac{1}{4}$  (see also Fig. 5).

The height of peaks (roughly) grows with  $h_f$  until  $h_f \approx 0.16$ , then except for the first peak the height decreases

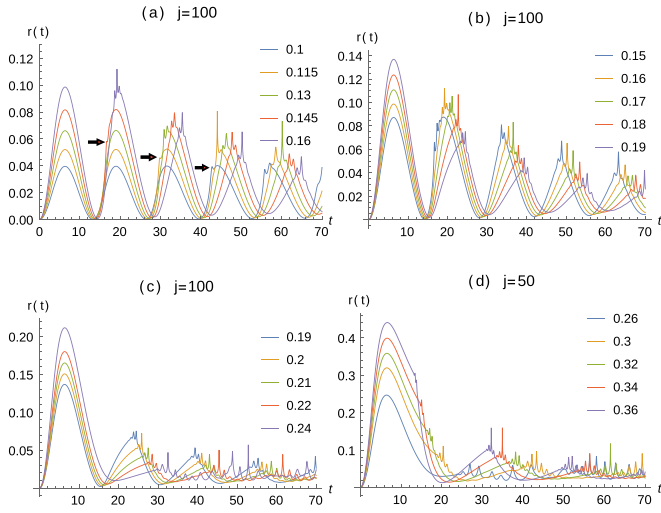


FIG. 19. The rate versus time. The Loschmidt rate  $r(t)$  as a function of time is displayed here in different colors for  $h_f = 0.1, \dots, 0.36$ , where  $h_{in} = 0$  in all the plots. Each sub-figure bears the value of  $j$  for which the plots are generated. (for more such plots, see [51,60,61,77,78]).

with the field's magnitude until  $h_f = \frac{1}{4}$ . Except the first peak, all peaks are lost and replaced by rapid oscillations in  $r(t)$  at the *dynamical* critical point  $h_f^{dy} = \frac{1}{4}$ . When we go beyond the critical point towards a higher  $h_f$  value, the kink occurs at the first peak [see Fig. 19(d)] and at an earlier time. It illustrates that  $\tau$  decreases towards 0 as we increase  $h_f$  from  $\frac{1}{4}$  to  $\infty$ . Moreover, in this range of  $h_f$ , the height of peaks rises with the field's strength. In the case of  $h_{in} = 0$ , the two phases of DPT-II are characterized by no kink (anomalous phase, when  $4h_f < 1$ ) or a kink (regular phase, when  $1 < 4h_f$ ) on the first peak before the first minimum of  $r(t)$  [60,75].

#### APPENDIX G: $T$ AND $\tau$ FOR $h_{in} \rightarrow \infty$ AND $h_f = 0$

Here we have  $|\psi_{in}\rangle = |j\rangle_x$ . For  $h_f = 0$ , the Hamiltonian  $H_f = -\frac{1}{2N}(J_z)^2$  is diagonal in the basis  $\mathcal{B}_z$  of (A2), and time-evolved ket (9) will be

$$|\psi(t)\rangle = \frac{1}{2^j} \sum_{m=-j}^j \binom{2j}{j+m}^{\frac{1}{2}} \exp\left(i \frac{m^2}{4j} t\right) |m\rangle_z. \quad (\text{G1})$$

With coherent ket (A3), one can check that  $|\psi(0)\rangle = |j\rangle_x$  and

$$|\psi(4j\pi)\rangle = \begin{cases} |-j\rangle_x & \text{when } j \in \mathbb{Z}, \\ |+j\rangle_x & \text{when } j \in \mathbb{Z} + \frac{1}{2} \end{cases} \quad (\text{G2})$$

up to a global phase factor, where  $\mathbb{Z}$  and  $\mathbb{Z} + \frac{1}{2}$  are the sets of integers and of half-integers, respectively. For an integer  $j$ , at the time  $t = 4j\pi$ , the phase factors in (G1) become  $\exp(i m^2 \pi) = +1$  and  $-1$  for an even and odd  $m$ , respectively. Therefore, we get  $|-j\rangle_x$  in (G2). When  $j \in \mathbb{Z} + \frac{1}{2}$ , all the magnetic quantum numbers are of the form  $m = k + \frac{1}{2}$ , where  $k \in \mathbb{Z}$ . Consequently,  $m^2 = k(k+1) + \frac{1}{4}$ , and all the phase factors are the same  $\exp(i m^2 \pi) = \exp(i \frac{\pi}{4})$  at  $t = 4j\pi$ , because  $k(k+1)$  is an even number. As a result, we get  $|+j\rangle_x$  in (G2).

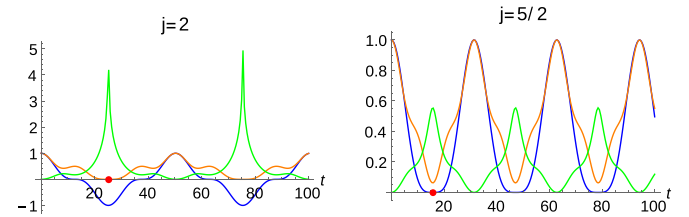


FIG. 20. The spin component, return probability, and rate versus time. The blue, orange, and green curves depict the  $x$  component of  $\mathbf{s}$ , the return probability  $p$ , and the Loschmidt rate  $r$  for  $h_{in} \rightarrow \infty$  and  $h_f = 0$ . The red points denote the half-time periods  $\frac{T}{2} = \tau$  given in (27).

Through (G2), we gain

$$\mathbf{x}(4j\pi) = \begin{cases} -1 & \text{when } j \in \mathbb{Z} \\ +1 & \text{when } j \in \mathbb{Z} + \frac{1}{2} \end{cases} \quad 0 \quad (\text{G3})$$

where  $\mathbf{x}$  is the  $x$  component of the spin vector  $\mathbf{s}$  of (10), and the return probability  $p$  is defined in (13). In fact, relations (G2) and (G3) hold true for any integral multiple of  $t = 4j\pi$  as the motion is periodic (see Fig. 20), and  $|\psi(8j\pi)\rangle = |+j\rangle_x$  when  $j \in \mathbb{Z}$ . Hence, we obtain the time period (27).

Furthermore, we acquire

$$\begin{aligned} \mathbf{x}(t) &= \frac{1}{j} \langle \psi(t) | J_x | \psi(t) \rangle \\ &= \frac{1}{j} \frac{1}{2^{2j}} \sum_m \binom{2j}{j+m} (j-m) \cos\left(\frac{2m+1}{4j} t\right) \\ &= \left(\cos \frac{t}{4j}\right)^{2j-1}. \end{aligned} \quad (\text{G4})$$

As per (G4), we have  $\mathbf{x}(2j\pi) = 0$  for all  $j \geq 1$ , and  $\mathbf{x}$  is a non-negative function of  $t$  for every  $j \in \mathbb{Z} + \frac{1}{2}$ . Since  $J_z$  commutes with the final Hamiltonian here, we get

$$\langle \psi(t) | J_z | \psi(t) \rangle = \langle \psi_{in} | J_z | \psi_{in} \rangle = 0,$$

$$\langle \psi(t) | (J_z)^2 | \psi(t) \rangle = \langle \psi_{in} | (J_z)^2 | \psi_{in} \rangle = \frac{j}{2}, \text{ and thus}$$

$$\mathbf{m} = 0 \quad \text{and} \quad \mathbf{m}' = \frac{1}{2j} \quad (\text{G5})$$

are the dynamical order parameters for every  $j$ .

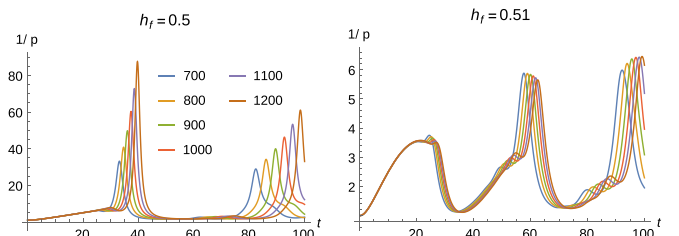


FIG. 21. Inverse probability versus time. Here  $|\psi_{in}\rangle = |j\rangle_x$ , and  $1/p$  of (13) is displayed in different colors for  $j = 700, \dots, 1200$ . In comparison to a rate versus time plot, one can see a kink rather distinctly in a  $1/p$  versus  $t$  plot such as this. In both the panels, the same color coding is used, while the values of  $h_f$  are written at the top.

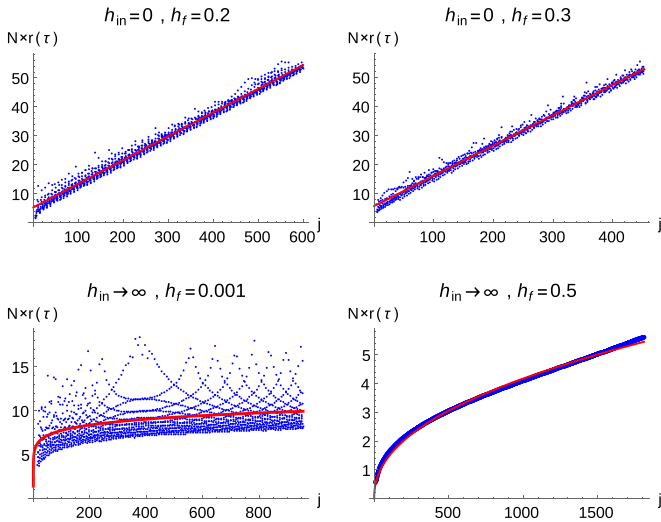


FIG. 22. Rate at the critical time versus system size. Plots in the top and bottom row are obtained by fixing  $|\psi_{\text{in}}\rangle = |j\rangle_z$  and  $|\psi_{\text{in}}\rangle = |j\rangle_x$ , respectively. The top- and bottom-pictures are associated with the plots in Figs. 7 and 12, respectively. At each picture we place the values of the field strength for which the exact data  $\{Nr(\tau_j)\}$  is obtained. Each data point is colored in blue, and the red curves show the best-fitted functions registered in Table V.

In the case of a half-integer  $j$ , we discover that the probability  $p$  reaches its global minima at the first time  $t = 2\pi j$  (see Fig. 20). Then the so-called Loschmidt amplitude becomes

$$\begin{aligned} \langle \psi_{\text{in}} | \psi(2\pi j) \rangle &= \frac{1}{2^{2j}} \sum_m \binom{2j}{j+m} \exp\left(i \frac{m^2}{2}\pi\right) \\ &= \frac{2^{j+\frac{1}{2}}}{2^{2j}} \exp\left(i \frac{\pi}{8}\right) \quad \text{and} \\ p(2\pi j) &= \frac{2^{2j+1}}{2^{4j}} \approx \frac{1}{2^{2j}} \quad \text{for } j \gg 1. \end{aligned} \quad (\text{G6})$$

In Fig. 20, one can see that the first kink in the return rate  $r(t)$  of (13) develops at the time  $\tau$  when the probability hits its

TABLE V. The best-fit functions for the rate at the critical time. This is the list of best-fit functions for the data  $\{Nr(\tau_j)\}$  presented in Fig. 22 and obtained through the least-squares method of Appendix E. The  $g$  functions are illustrated by the red curves in the figure.

$h_{\text{in}}$	$h_f$	$g(j)$	error
0	0.2	$(5.4 \pm 0.4) + (0.082 \pm 0.01) j^{(1\pm 0.02)}$	2.26
0	0.3	$(5.8 \pm 0.3) + (0.1 \pm 0.01) j^{(1\pm 0.02)}$	1.46
$\infty$	0.001	$(4.7 \pm 0.37) j^{(0.11\pm 0.013)}$	3.74
$\infty$	0.5	$(0.19 \pm 0.001) j^{(0.45\pm 0.001)}$	0.0051

lowest value. So, from (G3) and (G6), we deduce the value of  $\tau$  and report it in (27). Since  $p = 0$  in (G3), the rate diverges even for a finite  $j \in \mathbb{Z}$  (see Fig. 20). Whereas, for  $j \in \mathbb{Z} + \frac{1}{2}$ , we get  $r(2\pi j) \approx \ln(2)$  for  $j \gg 1$  from (G6). This completes the proof and discussion of (27).

## APPENDIX H: RATE AT THE CRITICAL TIME

Here we investigate the rate at the critical time  $r(\tau)$ . For  $h_{\text{in}} \rightarrow \infty$ , we plotted the inverse of the probability  $p(t)$  of (13) in Fig. 21. In the case of  $h_f = 0.5$ , one can observe that the peak at  $t \approx 38$  gets higher and sharper with the system size  $N = 2j$ . Whereas, in the case of  $h_f = 0.51$ , the peak around  $t = 23$  gets shorter and smoother with  $j$ . It demonstrates that there will be no kink in  $r(t)$  for  $h_f > \frac{1}{2}$  (the regular phase) [60,75,76].

Recall that the height of the first kink is  $r(\tau)$ , and we present the rescaled rate  $Nr(\tau) = \ln(\frac{1}{p(\tau)})$  in Fig. 22 for both Secs. III A and III B. In Table V, the best-fit functions for these data sets are given. In the case of Sec. III A, where  $h_{\text{in}} = 0$ , the data  $\{Nr(\tau_j)\}$  exhibit a linear behavior with  $j$ , which suggests  $\lim_{j \rightarrow \infty} r(\tau_j)$  goes to a nonzero value for both  $h_f = 0.2, 0.3$ . These two  $h_f$  values lie on the two sides of the dynamical critical point. In the case of Sec. III B, where  $h_{\text{in}} \rightarrow \infty$ , the best-fit function in Table V suggests  $Nr(\tau_j) \sim b j^c$  where  $0 < c < 1$ . It implies that  $\lim_{j \rightarrow \infty} r(\tau_j)$  goes to zero with a power law.

- 
- [1] S. Sachdev, *Quantum Phase Transitions* (Cambridge University Press, Cambridge 2011).
- [2] H. J. Lipkin, N. Meshkov, and A. J. Glick, *Nucl. Phys.* **62**, 188 (1965).
- [3] N. Meshkov, A. J. Glick, and H. J. Lipkin, *Nucl. Phys.* **62**, 199 (1965).
- [4] A. J. Glick, H. J. Lipkin, and N. Meshkov, *Nucl. Phys.* **62**, 211 (1965).
- [5] J. I. Cirac, M. Lewenstein, K. Mølmer, and P. Zoller, *Phys. Rev. A* **57**, 1208 (1998).
- [6] A. Micheli, D. Jaksch, J. I. Cirac, and P. Zoller, *Phys. Rev. A* **67**, 013607 (2003).
- [7] R. Botet, R. Jullien, and P. Pfeuty, *Phys. Rev. Lett.* **49**, 478 (1982).
- [8] R. Botet and R. Jullien, *Phys. Rev. B* **28**, 3955 (1983).
- [9] A. Das, K. Sengupta, D. Sen, and B. K. Chakrabarti, *Phys. Rev. B* **74**, 144423 (2006).
- [10] M. E. Fisher and M. N. Barber, *Phys. Rev. Lett.* **28**, 1516 (1972).
- [11] S. Hill and W. K. Wootters, *Phys. Rev. Lett.* **78**, 5022 (1997).
- [12] W. K. Wootters, *Phys. Rev. Lett.* **80**, 2245 (1998).
- [13] A. Shimony, *Ann. N.Y. Acad. Sci.* **755**, 675 (1995).
- [14] H. Barnum and N. Linden, *J. Phys. A: Math. Gen.* **34**, 6787 (2001).
- [15] M. B. Plenio and V. Vedral, *J. Phys. A: Math. Gen.* **34**, 6997 (2001).
- [16] D. A. Meyer and N. R. Wallach, *J. Math. Phys.* **43**, 4273 (2002).
- [17] T.-C. Wei and P. M. Goldbart, *Phys. Rev. A* **68**, 042307 (2003).
- [18] A. Osterloh and J. Siewert, *Phys. Rev. A* **72**, 012337 (2005).
- [19] A. Osterloh and J. Siewert, *Int. J. Quantum Inf.* **4**, 531 (2006).
- [20] R. Orús, *Phys. Rev. Lett.* **100**, 130502 (2008).

- [21] R. Orús, S. Dusuel, and J. Vidal, *Phys. Rev. Lett.* **101**, 025701 (2008).
- [22] R. Orús, *Phys. Rev. A* **78**, 062332 (2008).
- [23] M. Blasone, F. DellAnno, S. De Siena, and F. Illuminati, *Phys. Rev. A* **77**, 062304 (2008).
- [24] D. Z. Djoković and A. Osterloh, *J. Math. Phys.* **50**, 033509 (2009).
- [25] Q.-Q. Shi, R. Orús, J. O. Fjrestad, and H.-Q. Zhou, *New J. Phys.* **12**, 025008 (2010).
- [26] R. Orús and T.-C. Wei, *Phys. Rev. B* **82**, 155120 (2010).
- [27] A. Sen (De) and U. Sen, *Phys. Rev. A* **81**, 012308 (2010).
- [28] J. Vidal, G. Palacios, and R. Mosseri, *Phys. Rev. A* **69**, 022107 (2004).
- [29] S. Dusuel and J. Vidal, *Phys. Rev. Lett.* **93**, 237204 (2004).
- [30] S. Dusuel and J. Vidal, *Phys. Rev. B* **71**, 224420 (2005).
- [31] S. Dusuel and J. Vidal, *Phys. Rev. A* **71**, 060304(R) (2005).
- [32] J. I. Latorre, R. Orús, E. Rico, and J. Vidal, *Phys. Rev. A* **71**, 064101 (2005).
- [33] T. Barthel, S. Dusuel, and J. Vidal, *Phys. Rev. Lett.* **97**, 220402 (2006).
- [34] J. Vidal, S. Dusuel, and T. Barthel, *J. Stat. Mech.* (2007) P01015.
- [35] J. Wilms, J. Vidal, F. Verstraete, and S. Dusuel, *J. Stat. Mech.* (2012) P01023.
- [36] G. Liberti, F. Piperno, and F. Plastina, *Phys. Rev. A* **81**, 013818 (2010).
- [37] P. Calabrese, F. H. L. Essler, and M. Fagotti, *Phys. Rev. Lett.* **106**, 227203 (2011).
- [38] J. C. Halimeh, V. Zauner-Stauber, I. P. McCulloch, I. de Vega, U. Schollwöck, and M. Kastner, *Phys. Rev. B* **95**, 024302 (2017).
- [39] G. Piccitto, B. Žunkovič, and A. Silva, *Phys. Rev. B* **100**, 180402(R) (2019).
- [40] G. Piccitto and A. Silva, *J. Stat. Mech.* (2019) 094017.
- [41] M. Eckstein, M. Kollar, and P. Werner, *Phys. Rev. Lett.* **103**, 056403 (2009).
- [42] M. Schiró and M. Fabrizio, *Phys. Rev. Lett.* **105**, 076401 (2010).
- [43] M. Schiró and M. Fabrizio, *Phys. Rev. B* **83**, 165105 (2011).
- [44] M. Sandri, M. Schiró, and M. Fabrizio, *Phys. Rev. B* **86**, 075122 (2012).
- [45] B. Sciolla and G. Biroli, *Phys. Rev. Lett.* **105**, 220401 (2010).
- [46] M. Snoek, *Europhys. Lett.* **95**, 30006 (2011).
- [47] B. Sciolla and G. Biroli, *J. Stat. Mech.* (2011) P11003.
- [48] B. Sciolla and G. Biroli, *Phys. Rev. B* **88**, 201110(R) (2013).
- [49] A. Gambassi and P. Calabrese, *Europhys. Lett.* **95**, 66007 (2011).
- [50] P. Smacchia, M. Knap, E. Demler, and A. Silva, *Phys. Rev. B* **91**, 205136 (2015).
- [51] B. Žunkovič, A. Silva, and M. Fabrizio, *Philos. Trans. R. Soc. A* **374**, 20150160 (2016).
- [52] A. Lerose, B. Žunkovič, J. Marino, A. Gambassi, and A. Silva, *Phys. Rev. B* **99**, 045128 (2019).
- [53] B. Li, C. Gao, G. Xianlong, and P. Wang, *J. Phys.: Condens. Matter* **31**, 075801 (2019).
- [54] S. P. Kelly, E. Timmermans, and S.-W. Tsai, *Phys. Rev. A* **102**, 052210 (2020).
- [55] J. Zhang, G. Pagano, P. W. Hess, A. Kyprianidis, P. Becker, H. Kaplan, A. V. Gorshkov, Z.-X. Gong, and C. Monroe, *Nature (London)* **551**, 601 (2017).
- [56] J. A. Muniz, D. Barberena, R. J. Lewis-Swan, D. J. Young, J. R. K. Cline, A. M. Rey, and J. K. Thompson, *Nature (London)* **580**, 602 (2020).
- [57] K. Xu, Z.-H. Sun, W. Liu, Y.-R. Zhang, H. Li, H. Dong, W. Ren, P. Zhang, F. Nori, D. Zheng, H. Fan, and H. Wang, *Sci. Adv.* **6**, eaba4935 (2020).
- [58] S. Smale, P. He, B. A. Olsen, K. G. Jackson, H. Sharum, S. Trotzky, J. Marino, A. M. Rey, and J. H. Thywissen, *Sci. Adv.* **5**, eaax1568 (2019).
- [59] M. Heyl, *Phys. Rev. Lett.* **113**, 205701 (2014).
- [60] I. Homrighausen, N. O. Abeling, V. Zauner-Stauber, and J. C. Halimeh, *Phys. Rev. B* **96**, 104436 (2017).
- [61] J. Lang, B. Frank, and J. C. Halimeh, *Phys. Rev. B* **97**, 174401 (2018).
- [62] P. Jurcevic, H. Shen, P. Hauke, C. Maier, T. Brydges, C. Hempel, B. P. Lanyon, M. Heyl, R. Blatt, and C. F. Roos, *Phys. Rev. Lett.* **119**, 080501 (2017).
- [63] M. Heyl, A. Polkovnikov, and S. Kehrein, *Phys. Rev. Lett.* **110**, 135704 (2013).
- [64] M. Heyl, *Phys. Rev. Lett.* **115**, 140602 (2015).
- [65] J. C. Halimeh, M. Punk, and F. Piazza, *Phys. Rev. B* **98**, 045111 (2018).
- [66] U. Bhattacharya, S. Bandyopadhyay, and A. Dutta, *Phys. Rev. B* **96**, 180303(R) (2017).
- [67] S. Bhattacharjee and A. Dutta, *Phys. Rev. B* **97**, 134306 (2018).
- [68] N. Defenu, T. Enss, and J. C. Halimeh, *Phys. Rev. B* **100**, 014434 (2019).
- [69] R. Jafari, H. Johannesson, A. Langari, and M. A. Martin-Delgado, *Phys. Rev. B* **99**, 054302 (2019).
- [70] R. Jafari, *Sci. Rep.* **9**, 2871 (2019).
- [71] S. Zamani, R. Jafari, and A. Langari, *Phys. Rev. B* **102**, 144306 (2020).
- [72] S. Haldar, S. Roy, T. Chanda, A. Sen (De), and U. Sen, *Phys. Rev. B* **101**, 224304 (2020).
- [73] J. C. Halimeh, M. Van Damme, V. Zauner-Stauber, and L. Vanderstraeten, *Phys. Rev. Res.* **2**, 033111 (2020).
- [74] S. Porta, F. Cavaliere, M. Sassetti, and N. T. Ziani, *Sci. Rep.* **10**, 12766 (2020).
- [75] J. C. Halimeh and V. Zauner-Stauber, *Phys. Rev. B* **96**, 134427 (2017).
- [76] V. Zauner-Stauber and J. C. Halimeh, *Phys. Rev. E* **96**, 062118 (2017).
- [77] B. Žunkovič, M. Heyl, M. Knap, and A. Silva, *Phys. Rev. Lett.* **120**, 130601 (2018).
- [78] J. Lang, B. Frank, and J. C. Halimeh, *Phys. Rev. Lett.* **121**, 130603 (2018).
- [79] M. Heyl, *Rep. Prog. Phys.* **81**, 054001 (2018).
- [80] A. Sen (De), U. Sen, and M. Lewenstein, *Phys. Rev. A* **72**, 052319 (2005).
- [81] S. Deng, L. Viola, and G. Ortiz, in *Recent Progress in Many-Body Theories* (World Scientific, Singapore, 2008), Vol. 11, p. 387.
- [82] H. S. Dhar, R. Ghosh, A. Sen (De), and U. Sen, *Phys. Lett. A* **378**, 1258 (2014).
- [83] Y.-C. Lin, P.-Y. Yang, and W.-M. Zhang, *Sci. Rep.* **6**, 34804 (2016).
- [84] S. Haldar, S. Roy, T. Chanda, and A. Sen(De), *Phys. Rev. Res.* **2**, 033249 (2020).
- [85] C. M. Newman and L. S. Schulman, *J. Math. Phys.* **18**, 23 (1977).

- [86] F. T. Arecchi, E. Courtens, R. Gilmore, and H. Thomas, *Phys. Rev. A* **6**, 2211 (1972).
- [87] F. Pan and J. P. Draayer, *Phys. Lett. B* **451**, 1 (1999).
- [88] D. M. Greenberger, M. A. Horne, and A. Zeilinger, in *Bell's Theorem, Quantum Theory, and Conceptions of the Universe*, edited by M. Kafatos (Kluwer, Dordrecht, 1989), pp. 69–72.
- [89] X. Wang and K. Mølmer, *Eur. Phys. J. D* **18**, 385 (2002).
- [90] J. S. Kim, G. Gour, and B. C. Sanders, *Contemp. Phys.* **53**, 417 (2012).
- [91] H. S. Dhar, A. K. Pal, D. Rakshit, A. Sen(De), and U. Sen, in *Lectures on General Quantum Correlations and Their Applications*, edited by F. F. Fanchini, D. de Oliveira Soares Pinto, and G. Adesso, *Quantum Science and Technology* (Springer, Berlin, 2017), pp. 23–64.
- [92] W. Dür, G. Vidal, and J. I. Cirac, *Phys. Rev. A* **62**, 062314 (2000).
- [93] P. F. Byrd and M. D. Friedman, *Handbook of Elliptic Integrals for Engineers and Physicists* (Springer, New York, 1971), p. 11.
- [94] R. H. Dicke, *Phys. Rev.* **93**, 99 (1954).
- [95] D. M. Bates and D. G. Watts, *Nonlinear Regression Analysis and Its Applications* (Wiley, New York, 1988).
- [96] W. H. Press, S. A. Teukolsky, W. T. Vetterling, and B. P. Flannery, *Numerical Recipes: The Art of Scientific Computing* (Cambridge University Press, Cambridge, 2007).